# Supplementary Materials

## Materials and methods

### Data and Code Availability

Source code for data preprocessing and modeling and available at https://github.com/broadinstitute/pyro-cov. GISAID sequence data is publicly available at https://gisaid.org. PANGO lineage aliases are available at https://cov-lineages.org with source code at https://github.com/cov-lineages/lineages-website and lineage aliases available at https://github.com/cov-lineages/pango-designation. UShER phylogenies of public data are available at http://hgdownload.soe.ucsc.edu/goldenPath/wuhCor1/UShER_SARS-CoV-2. The whole genome map is available as part of NextClade at https://github.com/nextstrain/ncov/blob/50ceffa/defaults/annotation.gff. Structures of ORFab regions are available at https://www.ncbi.nlm.nih.gov/protein.

### Regression model of relative fitness ($PyR_0$ model)

We fit a Bayesian, hierarchical multinomial logistic regression model to data from GISAID using Pyro. Details are provided in the supplemental note below.

### Simulation of lineages

We carried out a simulation study to determine whether the process of clustering genomes into named lineages could generate an artifactual increase in estimated fitness. The simulation was of a single neutrally evolving viral population with discrete generations and a stochastic population size generated by a highly overdispersed negative binomial distribution with the current fitness. (Overdispersion parameter = 0.11, which yields 10% of cases causing 80% of transmission.) The fitness is 2.5 for the first 10 generations; subsequently it drops to 1.5 until the viral population reaches 80,000 infections, whereupon it drops again to 0.8. When the population decreases to 10,000, the growth switches back to 1.5, and continues cycling when the high and low population thresholds are reached. (A model with a roughly constant-sized population yields similar results.) The population starts as a single named lineage. Each generation, the most successful nodes in that generation are determined by looking ahead four generations and counting descendants. New lineages are assigned to the nodes with the most descendants (minimum of 200 descendants), up to a maximum of 10 lineages per generation. 10% of all infections are randomly sampled and any lineage with fewer than 20 descendants is discarded. When all new lineages have been generated and all nodes assigned a lineage, a global multinomial logistic regression is performed, using the Python package sklearn.linear_model, yielding relative fitness estimates of all lineages.

### Spatial analysis of mutation coefficients

To assess the spatial structure of the inferred amino acid coefficients $\beta_f$ (described in Probabilistic Model below), we utilize the Moran I spatial autocorrelation statistic. We report (see Table S1) one-sided p-values for Moran I computed using a permutation test with 999,999 random permutations. We use a gaussian weighting function of the form $\exp(-\text{distance}^2/\text{lengthscale}^2)$, where distance is measured in units of nucleotides. We compute Moran I statistics both for individual genes and the entire genome. For larger genes whose extent is 1000+ nucleotides we use a length scale of 50 nucleotides. For smaller genes (e.g. ORF8) we

set the length scale to one twentieth of the extent of the gene. When considering the entire set of amino acid changes, i.e. all 2,904 coefficients that make up $\beta_f$, we compute the Moran I statistic for two different length scales. We note, however, that the Moran I statistic is somewhat simplistic, since it is designed to pick up spatial structure at a single length scale. In particular it can be insensitive to complex spatial structure that involves multiple overlapping substructures at different scales. Nevertheless it offers a simple quantitative metric for identifying spatial structure in the coefficients $\beta_f$.

### Analysis of substitution statistics

To assess enrichment of amino acid changes we compared the event frequencies for the leading mutation sets (as determined by posterior mean/std ranking) against a background of all mutations used as features in the model using multiple testing corrected binomial tests. We performed this analysis for both the asymmetric case (where A->V and V->A are different events) and for the symmetric case.

### Comparison to other regression models

We fit logistic regression models in R version 4.0.3. The stats::glm() was used to fit binomial logistic regression models and the nnet::multinom function was used to fit multinomial logistic regression models. For multinomial logistic regressions, the data were filtered to contain sequences between January 1 2021 and December 31 2021 from the most common 25 pango lineages in the 10 countries with the most sequences available. The resulting dataset was downsampled to 10% of its initial size.

## Supplemental Note 1: Detailed description of $PyR_0$ model

### Data Preparation

We downloaded 6,466,300 samples from GISAID (*13*, *14*) on January 20, 2021. Each sample record includes labels for time, location, PANGO lineage annotation (*11*), and genetic sequence. We discard records with missing time, location, or lineage. We use UShER (*20*) to build a mutation-annotated phylogenetic tree, discarding sequences whose alignment quality is not reported as "good". We bin time intervals into 14-day segments, choosing a multiple of 7 to minimize weekly seasonality, but binning coarser than a week so as to reduce memory requirements; this results in 56 time bins.

Because sample counts vary widely across GISAID geographic region (by as much as five orders of magnitude), we aggregate regions into the following coarse partitions: each country counts as a region, and any first level subregion of a country counts as a region if it has at least 50 samples; otherwise it is aggregated into a whole-country bin. Note this means that e.g. a country may be split up into its larger regions, with smaller regions being subsumed into an aggregate country level bin. We then drop regions without samples in at least two different time intervals, resulting in 1560 regions in total. Figure S17 shows the distribution of samples among countries and GISAID regions.

After preprocessing, the model input data are a $T \times P \times C = 56 \times 1560 \times 3000$ shaped array $y_{tpc} \in \mathbb{N}$ of counts (this array is sparse and our inference code uses a sparse representation), and an $C \times F = 3000 \times 2904$ shaped array $X_{sf} \in \{0, 1\}$ of mutation features.

Cases per day (see Figure 3 inset) were estimated by multiplying confirmed case count data from Johns Hopkins University by the estimated proportion of each lineage within each (time, region) bin. We manually matched each GISAID region to the finest enclosing JHU region.

**Lineage Clustering**

Our method relies on a partitioning of genetic samples into clusters, where we estimate the fitness of each cluster. We initially tried to use the 1544 PANGO lineages as clusters, but found that some PANGO lineages appeared to include multiple distinct viruses of different fitness, e.g. B.1.1. exhibits two peaks in relative abundance in England, contrary to our multivariate logistic growth model. We therefore refined the 1544 PANGO lineages into 3000 finer clusters, with rates estimated individually for each cluster. Indeed Figure S4 shows that some PANGO lineages contain multiple distinct clusters of fitness estimates differing by more than a factor of two.

To create genetic clusters finer than PANGO lineages we began with a complete 4,833,238 node phylogeny of all GISAID samples maintained by Angie Hinrichs (*20*) (this phylogeny was created using UShER (*21*), excluding private mutations, masking difficult-to-sequence regions, eliding deletions, parsimoniously imputing missing sequence data). To coarsen the 4,833,238-node phylogenetic tree down to 3000 nodes (treated as clusters) we greedily collapsed parent-child edges, minimizing the the following distance function *TreeDistance*(-,-) between two mutation annotated trees

$$TreeDistance(T, T') = \sum_u \sum_v EditDistance(mrca(T, u, v),\ mrca(T', u, v)))$$

where T is the true mutation annotated tree, T' is the collapsed tree whose nodes we treat as clusters, u and v are sample sequences, *mrca*(T,u,v) is the sequence of the most recent common ancestor of u,v in the mutation annotated tree T, and *EditDistance*(-,-) counts amino acid substitutions between two sequences. This objective function minimizes the mean edit distance between the true mrca sequence and its cluster's sequence, for each pair of sequences. Changes in the objective function can be computed cheaply, and the O(n log(n)) time greedy algorithm can process the entire n=4,833,238 node phylogeny in under 5 minutes. Empirically this heuristic clustering produces trees that are approximately balanced in both cluster size and cluster-cluster edit distance, on both the true data and on synthetic datasets. Figure S18 shows the distribution of samples among both coarse PANGO lineages and the finer clusters. Figure S19 shows small example trees produced by clustering large synthetic trees.

**Probabilistic Model**

We model relative lineage growth with a hierarchical Bayesian regression model with a multinomial likelihood. Arrays in the model index over one or more indices: T=56 time steps (increments of 14 days) t; C=3000 clusters c; P=1560 regions ("places") p; and F=2904 amino acid substitutions ("features") f. The model, shown below, regresses lineage counts $y_{tpc} \in \mathbb{N}$ in each time-region-lineage bin against amino acid mutation covariates $X_{cf} \in \{0,1\}$. The variables y and X are observed and all other variables in the model are latent. Each latent variable is governed by a prior distribution. The full model is specified as follows (visualized in Figure S20), where the observed counts $y_{tpc}$ are underlined:

$$\alpha_c \sim \text{Normal}(0, \sigma_1) \qquad \sigma_1 \sim \text{LogNormal}(0, 2)$$

$$\alpha_{pc} \sim \text{Normal}(\alpha_c, \sigma_2) \qquad \sigma_2 \sim \text{LogNormal}(0, 2)$$

$$\beta_f \sim \text{Laplace}(0,\ \sigma_3) \qquad \sigma_3 = \frac{1}{2000}$$

$$\beta_{pc} \sim \text{Normal}\Big(\sum_f \beta_f X_{cf},\ \sigma_4\Big) \qquad \sigma_4 \sim \text{LogNormal}(-4, 2)$$

$$\underline{y_{tp.}} \sim \text{Multinomial}\Big(\sum_c y_{tpc},\ \text{softmax}(\alpha_p. + t\beta_p./\tau)\Big)$$

The proportion of lineages in a single time-region bin is modeled as a Multinomial distribution whose probability parameter is a multivariate logistic growth function $\text{softmax}(\alpha_{p\cdot} + t\beta_{p\cdot}/\tau)$ with intercept $\alpha_{pc}$ and slope $\beta_{pc}$ in units of generation time $\tau = 5.5$ days (these units are for interpretability only; the model does not use the notion of generation, and thus is robust to changes in generation time). Here the dot subscripts $\alpha_{p\cdot} \in \mathbb{R}^C$, $\beta_{p\cdot} \in \mathbb{R}^C$, and $y_{tp\cdot} \in \mathbb{N}^C$ denote vectors over cluster ids. The softmax function implements the multivariate generalization of logistic growth, inputting and outputting vectors, and is defined as

$$\text{softmax}(x)_i = \frac{\exp(x_i)}{\sum_j \exp(x_j)},$$

For a simple model of two lineages, each of the two components of the softmax function are sigmoid curves; however for more lineages, the functional forms may be more complex. Early iterations of the model used overdispersed likelihoods such as Dirichlet-Multinomial to account for additional variability not directly encoded in the generative process. However, we found that we can obtain much more accurate model predictions by using a Multinomial likelihood and accounting for model misfit by adding hierarchical structure elsewhere. The intercepts $\alpha_{pc}$ denote initial relative log prevalence of cluster c in region p; these are modeled hierarchically around the global relative log prevalence $\alpha_c$ of each cluster. The slopes $\beta_{pc}$ are modeled hierarchically around global per-cluster fitness $\Sigma_f \beta_f X_{cf}$ that are linearly regressed against amino acid substitution features $X_{cf}$. These linear coefficients $\beta_f$ can be directly interpreted as the effect of a mutation on a lineage's fitness, all other variation being equal. In figures we plot posterior means $\mathbb{E}[\beta_f | data] =: \Delta \log R$ as an estimate of effect size and plot the posterior z-score $|\mathbb{E}[\beta_f | data]| \,/\, \mathbb{V}[\beta_f | data]^{1/2} =: |\mu|/\sigma$ as a proxy for statistical significance.

Note that by regressing against amino acid changes we obviate the need to directly incorporate phylogenetic information into the model: if two lineages are close together in a phylogeny, then their amino acid features are likely also similar, so their regressed fitness values will likely be similar. By sharing statistical strength in this way we are also able to make accurate predictions for emergent lineages with few observations. (Note phylogenetic information is still used in preprocessing, since our clustering is created from an UShER phylogenetic tree.) Both of the hierarchies in $\alpha$ and $\beta$ empirically improve model fit in the presence of heavily skewed observations (e.g. most samples are from the UK, and there is a long tail of sparsely sampled regions). We chose these model structures based on extensive cross-validation and forecasting experiments.

We place weak priors on scale parameters $\sigma_1$, $\sigma_2$, and $\sigma_4$ (these denote standard deviations, the square roots of prior variance). The $\sigma_1$ and $\sigma_2$ priors are centered at large values to allow for wide variation in initial infection proportions across regions. The $\sigma_4$ prior is centered around the smaller value $e^{-4} \approx 0.018$ because we expect little variation of relative fitness across geographic regions a priori (some variation is expected, due to geographic variations in e.g. age distribution, behavior, or genetics as in binding affinity due HLA complex genotypes (*22*)). We fix the linear regression scale parameter $\sigma_3$ to a small value, forcing the regression problem towards a sparse solution (i.e. we assume a priori that most observed mutations have little effect on fitness). We choose a Laplace prior on regression coefficients because it is heavier-tailed than a Normal prior, but not so heavy-tailed that the regression problem becomes multimodal (as it would for e.g. a Cauchy or Student's t prior).

This proportional growth model differs from many forecasting models in the literature that are formulated in terms of absolute sample counts. Whereas our Multinomial likelihood allows us to model only the relative portions of lineages in each (time,region) bin, a Poisson likelihood would force us to additionally model the total number of genome samples in each (time,place) bin, a task which is less related to viral dynamics and more related to local lab capacity, political dynamics, and local calendars. We choose to model relative proportions rather than absolute counts because the relative model is robust to a number of sources of bias, including: sampling bias across regions (e.g. one region samples 1000x more than another); sampling bias over time (e.g. change in sampling rate over time); and change in absolute fitness of all lineages, in any (time, region) bin (e.g. due to changes in local policies or weather, as long as those changes affect all lineages equally). However the model is susceptible to the following sources of bias: biased sampling in any (time, region) cell (e.g. sequencing only in case of S-gene target failure); and changes in sampling bias within a single region over time (e.g. a country has a lab in only one city, then spins up a second lab in another distant city with different lineage proportions).

This model has several advantages over existing approaches. First, it provides a principled, agnostic approach that can be applied to a large dataset to identify lineages that demonstrate concerning epidemiological features. Second, by modeling the relative fitness of lineages separately across 1560 geographic regions, the model is robust to region-specific differences in non-pharmaceutical interventions and vaccination rates. Third, the hierarchical nature of the model which represents lineages as collections of mutations reflects the underlying biology and yields both strain- and lineage-specific coefficients from a single inferential approach. While the linear-additive model of mutation biology is a coarse approximation to true biology including epistasis, our hierarchical model serves as a framework to explore such models (*23*, *24*) on SARS-CoV-2 genomic surveillance data.

We interpret the regression coefficients as the relative fitness based on a well-known result in population genetics (Crow and and Kimura 1970) that the change in genotype frequency in a large haploid population under selection follows a logistic curve, where the logistic growth rate parameter defines the relative fitness of genotypes.

**Probabilistic Inference**

The model is implemented in the Pyro probabilistic programming language (*15*) built on PyTorch (*25*). To fit an approximate joint posterior distribution over all latent variables (a space of dimension 375,909), we train a flexible reparameterized variational distribution using stochastic variational inference. Our variational approach starts by reparameterizing the model

via a sequence of learnable but distribution-preserving decentering transforms (*26*) on the α and β latent variables. Reparameterizing is particularly helpful in avoiding Neal's-funnel situations (*27*) by smoothing out the geometry of latent variables with Normal prior whose scale parameter is also a latent variable. After reparameterizing we model the posterior over all variables as a joint multivariate Normal distribution whose covariance matrix $\mathbf{\Sigma}$ is parametrized by a rank-200 matrix plus a diagonal matrix $\mathbf{D}$ with positive entries:

$$\mathbf{\Sigma}_{ij} = \sum_{\ell=1}^{200} \mathbf{\Lambda}_{i\ell}\mathbf{\Lambda}_{j\ell} + \boldsymbol{D}_{ij}$$

where $\mathbf{\Lambda}$ is an unconstrained matrix of size 375,909 x 200. This low-rank multivariate Normal distribution allows the approximate posterior to capture correlated uncertainty among competing mutations each of which might explain increased fitness. This variational distribution has 75,936,525 parameters to be optimized (much larger than the number 375,909 of latent variables, but much smaller than the $375{,}909 \times (375{,}909 + 1) / 2 \cong 7 \times 10^{10}$ parameters that would be required to represent a full-rank covariance matrix).

Variational inference is performed for 10,000 iterations with the Adam optimizer (*28*) with clipped gradients and an exponentially decreasing learning rate schedule and initial learning rates between 0.05 and 0.0025 for different parameter groups (see Figure S21). Optimization proceeds in batch-mode, i.e. without any data subsampling. We initialize model parameters to median prior values with a small amount of noise added to avoid scale parameters collapsing early in training. After inference we make predictions by drawing 1000 posterior samples. See source code for detailed optimizer and initialization configuration.

Inference and prediction on a single GPU (NVIDIA Tesla A100 with 48GB of RAM) takes about 10 minutes (compared to 14.5 hours on an 8-core CPU), which is less than the amount of time required to download and preprocess each daily snapshot of data from GISAID. The cost of fitting the model is O((TP+F)C), dominated by pointwise mathematical operations, particularly computing the softmax function on a dense array of shape T×P×C. This cost does not depend directly on the number of genetic samples, since samples are aggregated into counts y of constant shape T×P×C.

We emphasize that inference in this model is very challenging due to the large dimension of the latent space (namely 375,909), itself a consequence of the large number of regions, lineages, and mutations considered by the model (*29*). While variational inference has a number of attractive features, especially computationally, like any approximate inference scheme it comes with disadvantages. In our case the most notable disadvantage of variational inference is its tendency to yield biased posterior uncertainty estimates. Typically posterior uncertainty is underestimated, leading to credible intervals (CI) that in some cases can be unrealistically narrow. The primary parameters of interest in the $\mathrm{PyR}_0$ model are the mutation-level coefficients $\beta_f$ and the per-lineage fitness values $\Sigma_f \beta_f X_{cf}$. Since the latter quantity governs the prior over $\beta_{pc}$, which in turn directly feeds into the multinomial likelihood, the per-lineage fitness estimates are more-or-less tightly constrained by the observed counts $y_{tpc}$. Consequently the posterior uncertainty of per-lineage fitness is comparatively easy to estimate and we expect variational inference to yield reasonable credible intervals for these quantities. In contrast the mutation-level coefficients $\beta_f$ interact with correlated features $X_{cf}$ (leading to a multi-modal posterior) and are less directly constrained by the observed counts $y_{tpc}$. Consequently it is significantly more challenging to estimate the

corresponding posterior uncertainty. In practice we obtain implausibly narrow credible intervals for these quantities and the posterior uncertainty must be interpreted with caution. Importantly, while the uncertainty estimates for $\beta_f$ should not be taken at face value, we believe that they are still very useful for interpreting inferred model parameters, since they *can be used to rank/prioritize different hits* $\beta_f$. In particular, while the absolute magnitudes of $\beta_f$ uncertainty estimates are implausible, their *relative magnitudes* are representative of the amount of supporting evidence, and thus are useful for ranking. Since we consider a large number of mutations (F=2904) this information is invaluable for designing experiments for functional characterization.

**Implementation**

We implemented the $PyR_0$ model using the probabilistic programming language Pyro (*15*). The model leverages PyTorch and Pyro to scale efficiently to large data sets and can therefore be applied continuously as datasets grow, completing model training and prediction with millions of viral genomes in minutes on a single GPU. We chose the Pyro framework because it cleanly separates model specification from inference customization, and scales to large models and datasets by leveraging GPUs. This flexible modeling framework allowed us to experiment with different hierarchical structures. Additionally by relying on an open source and well-tested modeling and inference framework, we minimize the risk of introducing software bugs into our analysis. The speed of inference—which took about 10 minutes on a single GPU on the full dataset of >6 million genomes—allowed quick model iteration and thorough validation on subsets of the data, including both geographic cross-validation and temporal data truncation.

**Prediction**

In Figure 3, the 95% confidence intervals in parentheses were estimated by drawing 1000 samples from the variational posterior distribution. Confirmed cases per day were estimated at the end of the training period (Jan 20 2021) by combining our model's relative lineage portions with confirmed case count data from Johns Hopkins university. Quantities defined over our 3000 fine clusters were aggregated up to coarser PANGO lineages for reporting. To facilitate downstream use of model predictions we have provided complete tables of lineage fitness estimates (Data S1) and mutation coefficients (Data S2). These predictions have been used e.g. by Nextstrain.org to visualize our predicted mutational fitness along a phylogenetic tree (Figure S22).

**Validation**

We considered the possibility of biased submission to the GISAID database and compared results obtained from the full dataset with results obtained from disjoint subsets. For this purpose we divided the data into samples from the most heavily sampled region (Europe, with 3.3M samples) and those from the rest of the world (with 3.1M samples) (Figures S1,S11). This split is motivated by most samples originating from the UK: we widened the region around the UK until the region and its complement both had roughly equivalent statistical strength and narrow posterior estimates. We conducted two-fold cross-validation experiments for both lineages (Figure S1) and mutations (Figure S11). Additionally, in Figure S23, we show that $PyR_0$ lineage-level $\Delta$ log R estimates are largely driven by regions with the largest numbers of samples and are thus robust to the manner in which under-sampled regions are organized into spatial units.

We found the full GISAID dataset to be invaluable to making accurate predictions. Using data up to July 2021, we tried restricting to either all CDC data or CDC's randomly sampled NS3 dataset and found those subsets to result in insufficient diversity and lead to unclear results (Pearson correlation 0.49, 0.28, respectively). Using data snapshots from mid January 2022, we tried restricting to open data available in GENBANK, but found the model made implausible estimates of Omicron fitness, due to a combination of lack of geographic diversity (GENBANK has only about 1/10 as many geographic regions as we were able to extract from GISAID data, and particularly has very few samples from South Africa) and data upload latency (GISAID appeared to have ~1 week upload latency, versus ~1 month for GENBANK).

Our model assumes each single point mutation independently linearly contributes to change in fitness. A natural generalization is to search for groups of mutations that affect fitness. To explore this we fit a similar model of both single and pair mutations, considering only pairs that lie within the same gene. Fitting this model on data up to July 2021, we discovered no pairwise mutations stronger than the top 100 single mutations. While these experiments did not discover pairwise mutations, we believe that more sophisticated models would be able to measure epistasis, but sophistication in that area is beyond the scope of the present work.

Finally, to compare our multinomial multivariate logistic growth model to simple binomial univariate logistic growth, we compared lineage fitness estimates (Figure S24) and logistic growth curves (S25) of all but one lineage at a time, showing good agreement on the narrow selection of lineages examined by each binomial logistic fit.

**Supplemental Note 2:**

**Cell culture**

Cells were cultured in humidified incubators with 5% $CO_2$ at 37º C, and monitored for mycoplasma contamination using the Mycoplasma Detection kit (Lonza LT07-318). HEK293 *Homo sapiens*, female, embryonic kidney cells (ATCC CRL-1573) were cultured in DMEM supplemented with 10% heat-inactivated FBS, 1 mM sodium pyruvate, 20 mM GlutaMAX, 1× MEM non-essential amino acids, and 25 mM HEPES, pH 7.2.

**Virus production**

24 hrs prior to transfection, $6 \times 10^5$ HEK-293 cells were plated per well in 6 well plates. All transfections used 2.49 µg plasmid DNA with 6.25 µL TransIT LT1 transfection reagent (Mirus, Madison, WI) in 250 µL Opti-MEM (Gibco). Single-cycle HIV-1 vectors pseudotyped with SARS-CoV-2 Spike protein, either D614 or D614G, were produced by transfection of either HIV-1 pNL4-3 Δenv Δvpr luciferase reporter plasmid (pNL4-3.Luc.R-E-), or pUC57mini NL4-3 Δenv eGFP reporter plasmid, in combination with the indicated Spike expression plasmid, at a ratio of 4:1. ACE2 expression vectors were produced by transfecting cells with one of the pscALPSpuro-ACE2 plasmids, along with the HIV-1 *gag-pol* expression plasmid psPAX2, and the VSV glycoprotein expression plasmid pMD2.G (4:3:1 ratio of plasmids). 16 hrs post-transfection, culture media was changed. Viral supernatant was harvested 48 hours after media change, passed through a 0.45 µm filter, and stored at 4ºC. TMPRSS2 expression transfer vector was produced similarly but with pscALPSblasti-TMPRSS2.

**Generation of cell lines expressing ACE2 and TMPRSS2**

$2.5 \times 10^5$ HEK-293 cells were plated per well in a 12 well plate. The next day cells were transduced with 250 uL of supernatant containing TMPRSS2-encoding lentivirus for 16 hr at

37°C, after which fresh media was added to cells. 48 hrs after transduction cells were replated and selected with blasticidin (InvivoGen, catalogue #ant-bl-1) at 10 ug/ml. After selection, cells were transduced similarly with supernatant containing ACE2-encoding lentivirus and selected with 1 ug/mL of puromycin (InvivoGen, San Diego, CA, catalogue #ant-pr-1).

**Virus Infectivity Assays**

16 hours prior to transduction, adherent cells were seeded in 96 well plates. HEK-293 cells were plated at 5 x $10^4$ cells per well. Cells were incubated in virus-containing media for 16 hrs at 37°C when fresh medium was added to cells. 48 to 72 hours after transduction cells were assessed for luciferase activity. Cells transduced with luciferase expressing virus were assessed using Promega Steady-Glo system (Promega Madison, WI). GraphPad Prism 8.4.3 was used to analyze the infectivity data using a ratio paired t test. In these experiments, all values shown are the mean with standard deviation, with the actual calculated two-tailed *P* value indicated.

**Supplemental Note 3:**

We include here an extended discussion of high-scoring mutations.

**Relation to other viruses**

The concentration of putative transmission-promoting substitutions in N at positions 160-210 is remarkable, but is supported by a similar observation in Ebola virus(*30*), and recent data for SARS-CoV-2 showing mutations in that region increase the efficiency of viral packaging(*31*), validating some of the model's most unexpected predictions and supporting its ability to identify novel biology.

**Potential functional roles of mutations within ORF1**

Our model highlighted mutations within the ORF1 non-structural proteins (nsps) whose functions are not fully understood (e.g. Table S3). We found two predominant clusters within ORF1a: one in the C-terminal ~120 amino acids of nsp4 and the other within the N-terminal ~160 amino acids of nsp6 (Figure S13C). Nsp4 and nsp6 are both membrane-anchored proteins with roles in assembly and concentration of the viral replication and transcription complex (RTC) machinery within double-membrane vesicles (*32*). Amino acid substitutions in these regions, combined with transmission-associated mutations identified within additional RTC-associated nsps (e.g., nsp12-16, Figure S13D), may therefore affect the kinetics of replication and gene expression, resulting in higher virus yields from infected cells. Nsp2, a rapidly evolving accessory protein (*33*)(*34*)(*35*) whose proposed function in disrupting host cell signaling (*36*) and viral mRNA translation initiation (*37*) remains obscure, harbored many additional mutations associated with higher fitness (Figure S13C).

The ORF1a-ORF1b polyprotein is processed into 16 non-structural proteins by two viral proteases: a papain-like protease (nsp3) and 3C-like protease (nsp5). Multiple transmission-associated mutations were found within the protease coding regions (e.g., ORF1a:V1750A, ORF1a:P3395H). Most of the amino acid substitutions identified by our model were outside of the domains containing catalytic residues for nsp3 (C1674, H1835, D1849) or nsp5 (H3304, C3408) (*38*)(*39*). However, the potential effects of these mutations on protease architecture and activity warrant further experimentation. A few of the top mutations from our model (e.g., ORF1a:T3255I, ORF1a:A3571V) are positioned adjacent to nsp cleavage sites, potentially influencing local structures and kinetics of polyprotein processing by nsp3 and nsp5 (Figure S13C-D).

Multiple highly-ranked mutations are distributed across the replication and transcription-associated nsps in ORF1b (Figure S13D). The P314L (P323L) mutation in nsp12 – the viral RNA-dependent RNA polymerase (RdRP) – emerged early during the pandemic and became established in circulating lineages alongside S D614G (*6*). A later variant at this site (P314F) was also highly ranked in our list. Additional mutations in nsp12 can be found within the canonical fingers (D445A, V631I, D514N, G662S), palm (M592I, H604Y, T701I, C721R, S763F), and thumb (L820F, L829I, D870N) subdomains of the RdRP conserved catalytic fold (Figure S15). The functional effects of these mutations on polymerase processivity and fidelity remain to be investigated. A structural model of the SARS-CoV-2 polymerase complex has been resolved (*40*)(*41*), and contains a single subunit of nsp12, two subunits of the nsp13 helicase, and additional RdRP cofactor proteins (nsp7, 8, and 9). The ORF1b P314 residue is located at the

interaction interface between nsp12 and a single subunit of nsp8. Moreover, several of the top mutations from our dataset ORF1b (e.g., P1000L, P1001S, Q1011H) are harbored within the nsp13 N-terminal zinc-binding domain that directly interacts with nsp8 (*42*). These findings implicate transmission-associated mutations within the SARS-CoV-2 RNA synthesis machinery in altering the stability of the replication complex, possibly via interactions with nsp8.

Nsp14 is a dual-functional enzyme with N-terminal 3'-to-5' exonuclease (ExoN) and C-terminal guanine-N7 methyltransferase (N7-MTase) activities (*43*)(*44*) and is a core component of the coronavirus RNA proofreading complex. Nsp14 is uniquely responsible for excision of mismatched bases from the nascent RNA and methylation of the viral mRNA cap structure. Two mutational hotspots in nsp14 map to discrete regions in the ExoN (e.g., T1540I, I1566V) and N7-MTase (e.g., D1848Y, P1936H) domains. The functional consequences of these clusters of transmission-associated mutations on mRNA synthesis and genome replication remain unknown.

## Supplementary Figures

A.

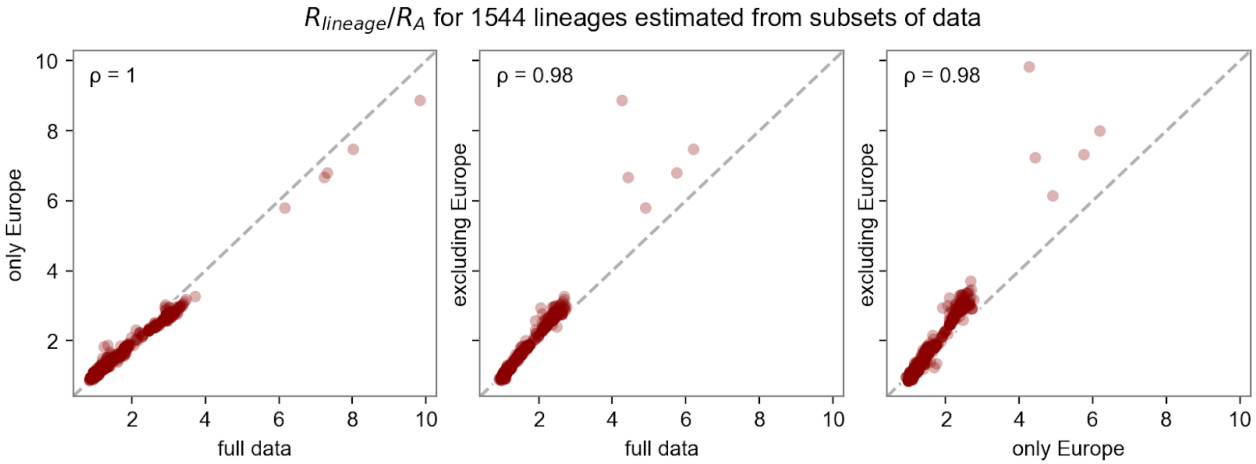


B.

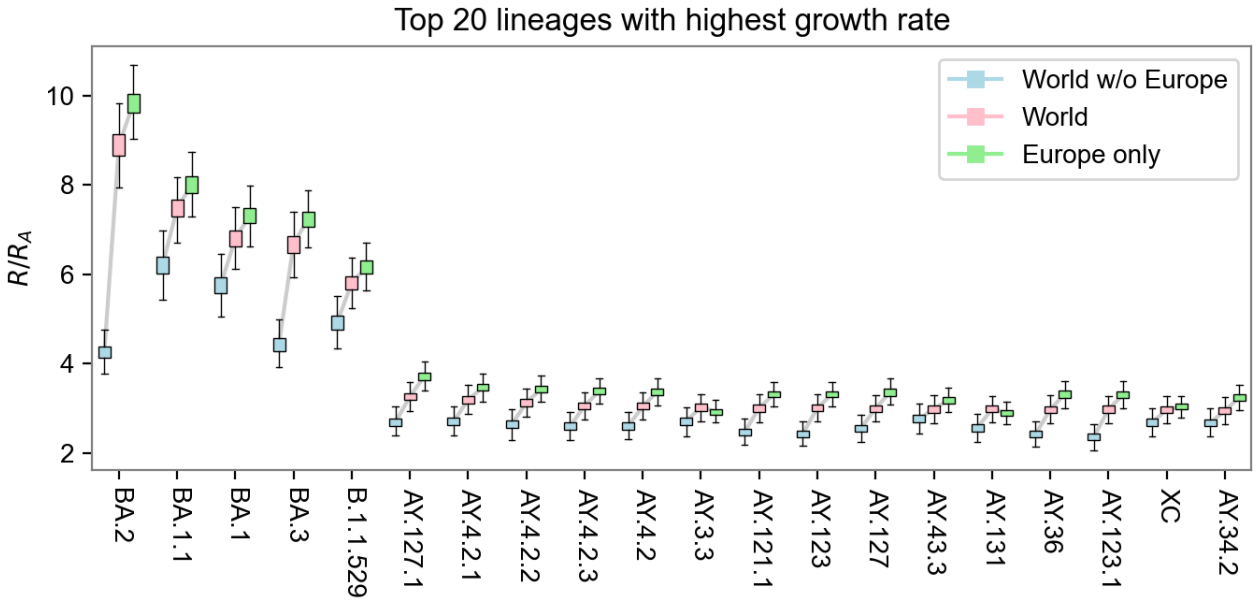


**Figure S1. A**. Sensitivity of lineage fitness estimates to data subset. We depict the relative fitness of all lineages as estimated by either the full data or two disjoint geographic subsets (within Europe and outside Europe). High Pearson correlation (ρ) suggests estimates are largely insensitive to data subset. **B**. Estimates of fold increases in fitness for the top 20 lineages. Sensitivity analysis shows consistency across estimates from subsets of the data in different geographic regions.

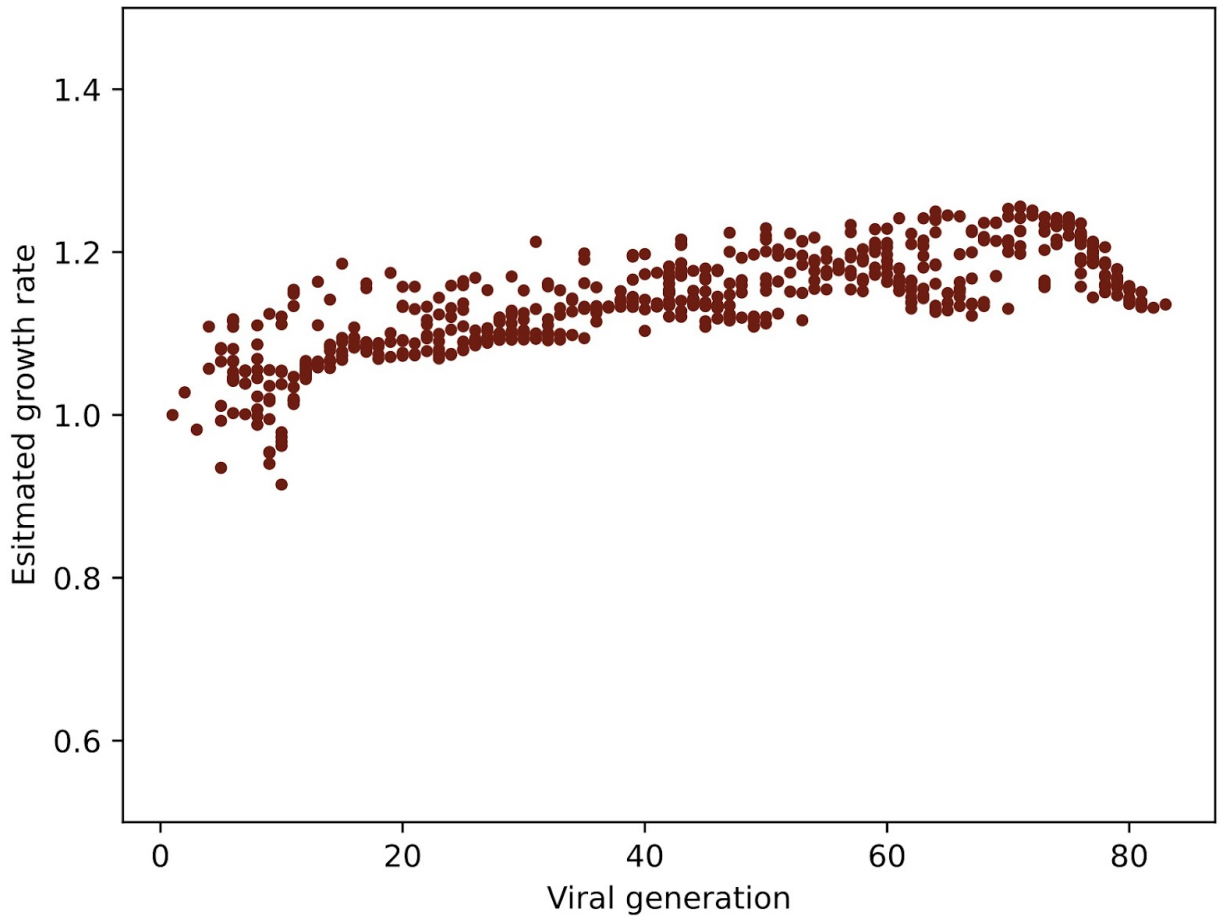


**Figure S2.** Simulation study assessing bias. Distribution of inferred fitness of new lineages as a function of time, for a simulated neutrally evolving viral population. The most successful subclades of each generation are designated as new lineages, leading to a trend toward higher estimated fitness even though all lineages are equally transmissible.

**A.**

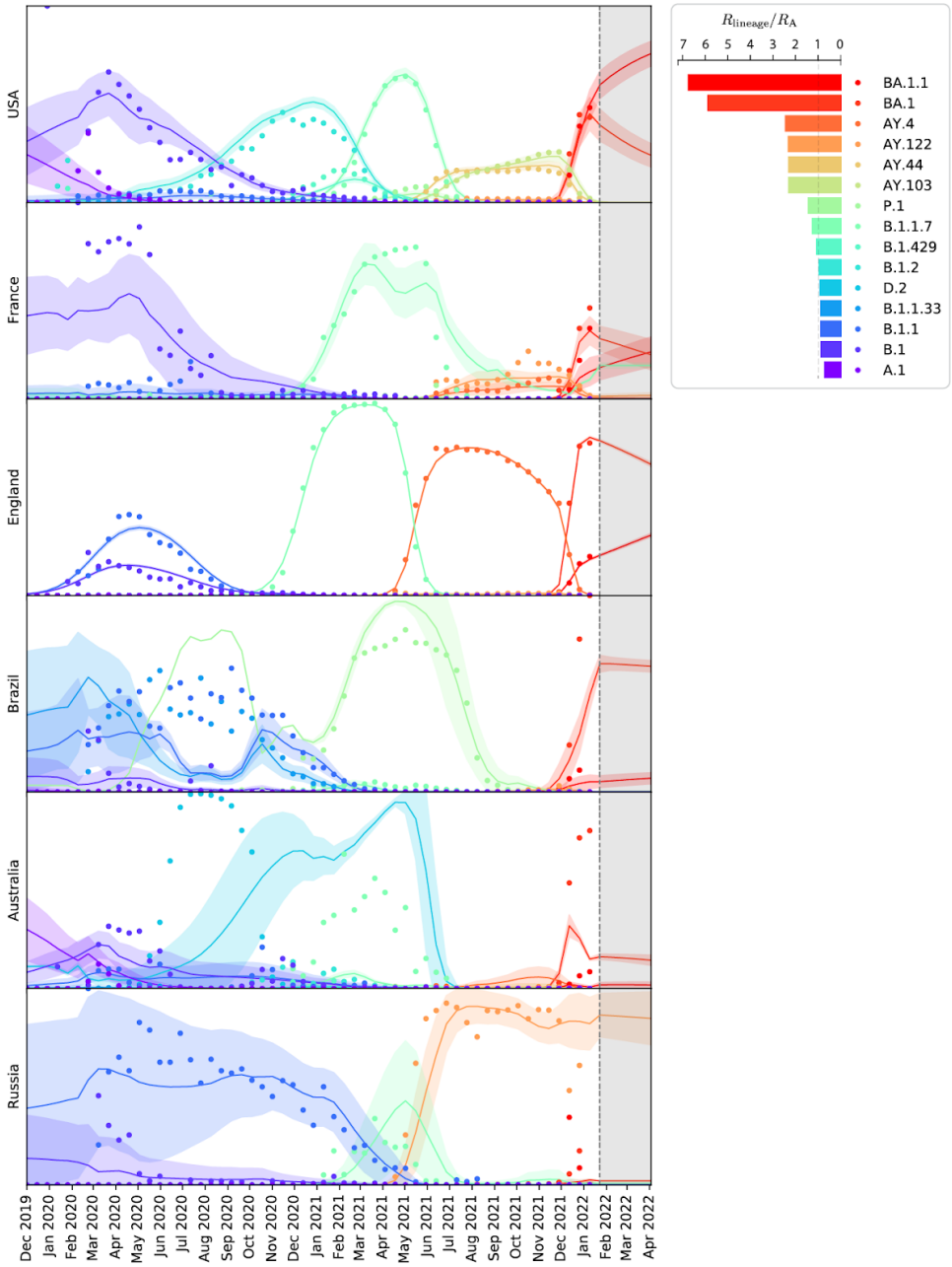

**B.**

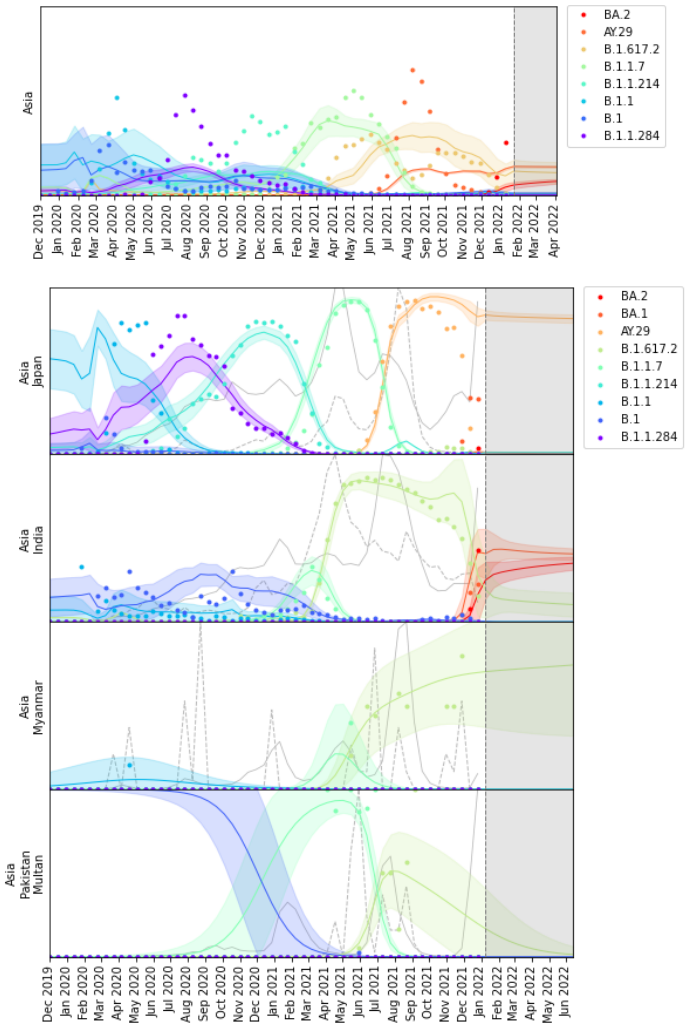


**Figure S3**. **A.** Regional fits and forecasts for USA, France, England, Brazil, Australia and Russia. Solid circles at the beginning of each two week time interval denote observed lineage proportions on a [0, 1] scale for the top 20 lineages. Solid curves and 95% confidence bands denote model predictions and three-month forecasts. Each of the six (aggregate) regions is made up of multiple subregions. The behavior of each SARS-Cov-2 cluster in each subregion is represented by only two numbers in the model: a slope and an intercept. The complex model fit results from the multivariate logistic function applied jointly to multiple competing trends, which are then aggregated over subregions and multiple clusters per lineage. England shows clear waves of dominance: B.1.1, B.1.177, B.1.1.7 (Alpha), AY.4 (Delta), and finally BA.1 (Omicron), with the latter currently being overtaken by BA.1.1 (also Omicron). Massachusetts and Brazil both start with very low sampling rates early in the pandemic. The legend reports the estimated fitness for the top 15 lineages. **B.** Region-specific fits for several regions in Asia, demonstrating better fits in regions with high sampling (Japan, India), and degraded fits in regions with low sampling (Myanmar, Pakistan).

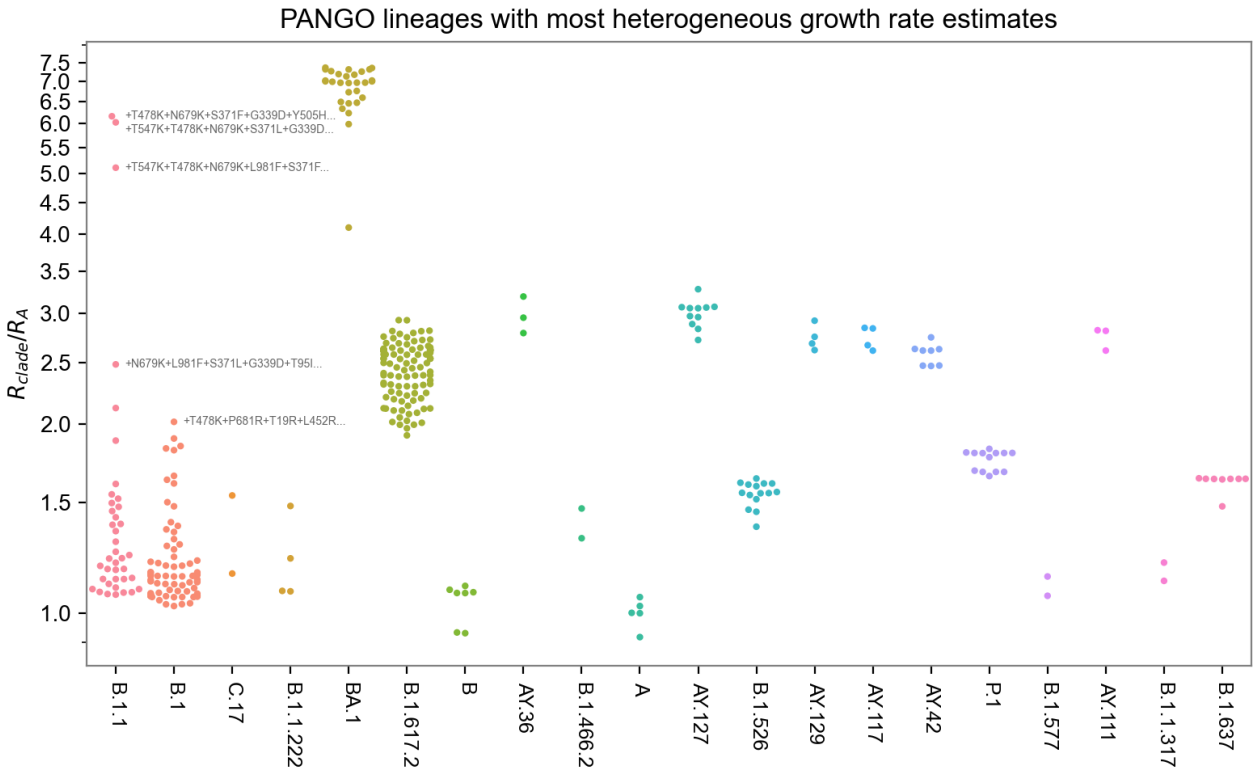


**Figure S4.** Heterogeneity of PANGO lineages. We hypothesized that the PANGO lineage clustering conflated viruses with distinct growth rate, e.g. B.1.1 exhibits two peaks in relative abundance in England, contrary to our multivariate logistic model. To test this hypothesis we refined 1544 PANGO lineages into 3000 finer clusters and estimated each cluster's growth rate. As shown in the figure some PANGO lineages include clusters with estimated fitness differing by more than a factor of 6, including the B.1.1 lineage. This heterogeneity is also reflected in the temporal structure: for example, the three B.1.1 clusters with the largest growth rate emerged in December 2021 and January 2022, whereas the majority of B.1.1 clusters emerged in the twelve months leading up to April 2021. The top four clusters in B.1.1 and the top cluster in B.1 are labeled by their top 5 fitness-increasing mutations to the S gene, relative to the PANGO lineage's basal sequence.

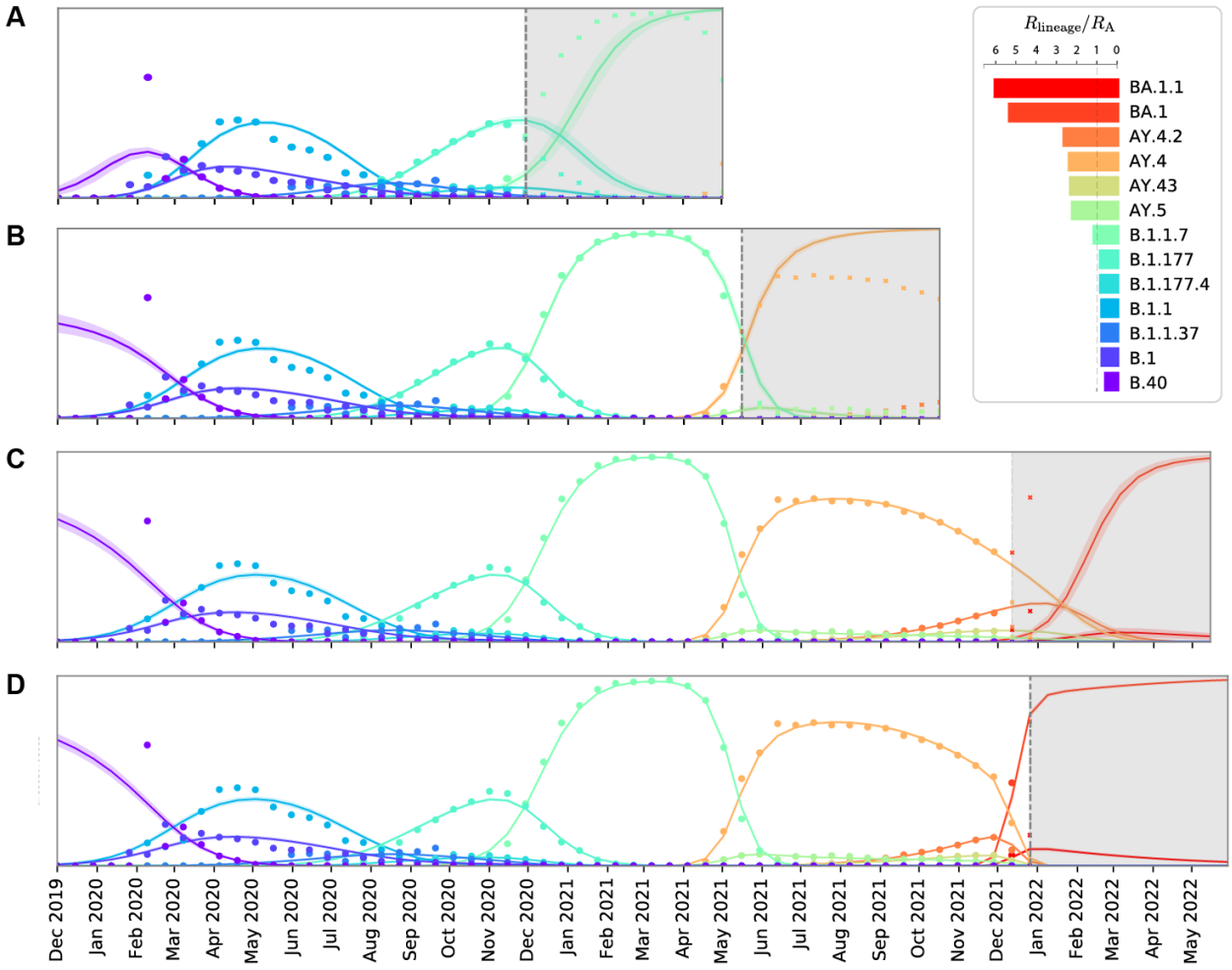


**Figure S5.** Forecasts in England with time-truncated input data. (A) Prediction for rise of B.1.1.7 using data through late November 2020 (solid circles at the beginning of each two-week time interval). (B) Prediction for rise of AY.4 using data through early May 2021. (C) Prediction for rise of BA.1 using data through mid December 2021, and (D) late December 2021. Future data points, not used during the model training, are shown in crosses. The legend reports lineage fitness estimates based on all available data.

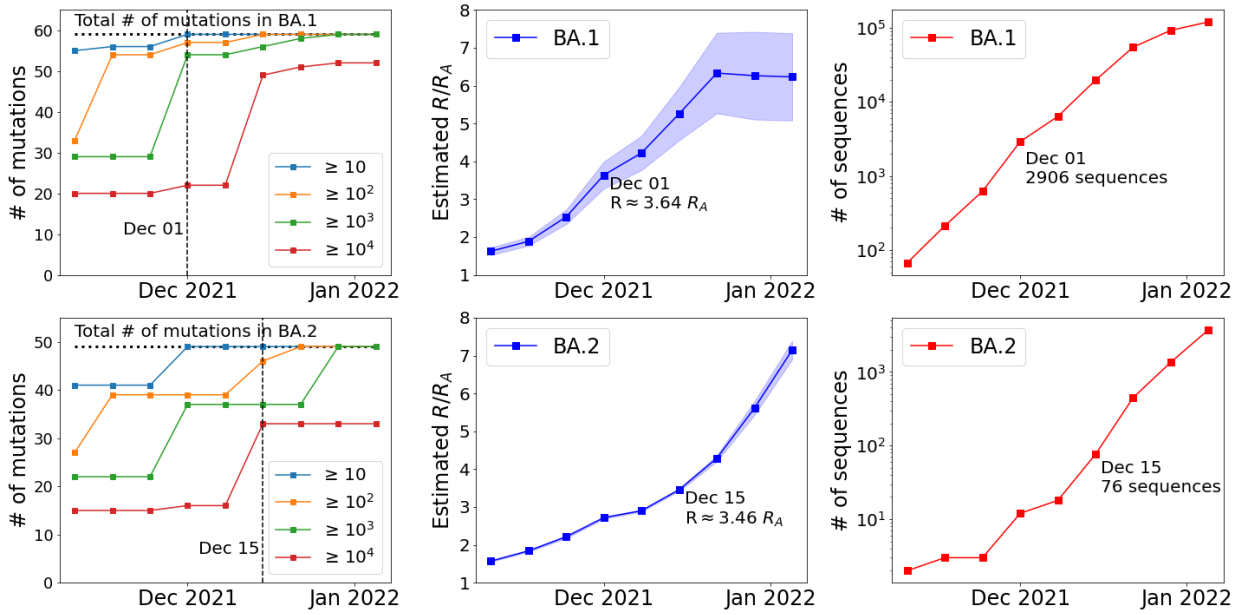


**Figure S6**. We depict the ability of $PyR_0$ to predict the fitness of Omicron sublineages BA.1 and BA.2 as the number of sequenced genomes increased throughout the last two months of 2021. $PyR_0$ predicted that BA.1 (respectively, BA.2) was substantially more fit than Delta by December 1st (15th) 2021, by which time 2906 (76) genomic sequences had been collected. The substantial heterogeneity of the BA.1 sublineage is reflected in the uncertainty in BA.1 R estimates; this heterogeneity also helps explain why $PyR_0$ required more sequences to identify the elevated fitness of BA.1 as compared to the case of BA.2. **Left:** The number of amino acid mutations that make up BA.1 and BA.2 that had been observed in at least $10/10^2/10^3/10^4$ sequences by the given date. **Middle:** Estimates of $R/R_A$ using sequences collected by the given date. **Right:** The total number of BA.1 and BA.2 sequences collected by the given date.

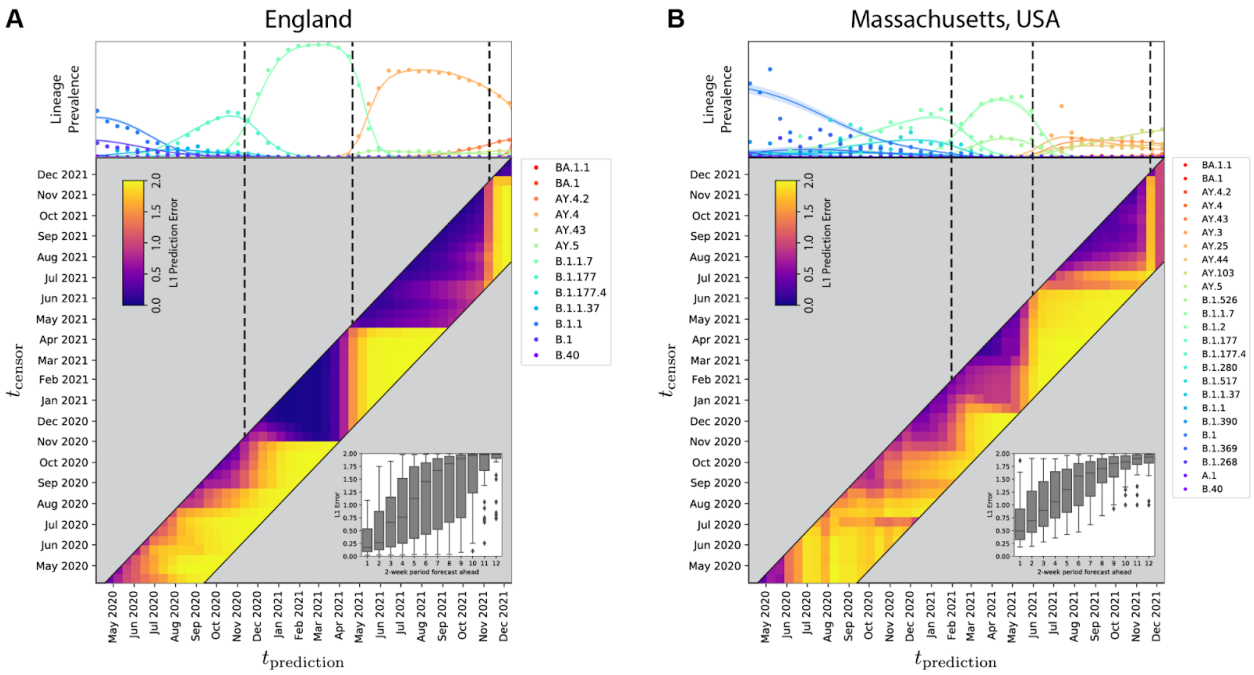


**Figure S7**: Forecasting evaluation based on independently trained models at 45 time points during the pandemic, $t_{censor}$, and predicting at time $t_{predicted}$ up to 12 two-week periods into the future. The results are shown for (A) England and (B) Massachusetts, USA. The top panels are as in Figure S3, heatmaps depict the prediction L1 error, and the inset bar plots depict the aggregated prediction errors over all periods. Note the rapid increase in error as new fit lineages emerge in a region (vertical dashed lines provided as a guide to the eye), followed by rapid recovery and stabilization of forecasting accuracy within only a single period, highlighting the predictive value of $PyR_0$ for detecting variants of concern. Refer to Table S1 for tabulated forecasting accuracy figures in several other regions.

## Figure

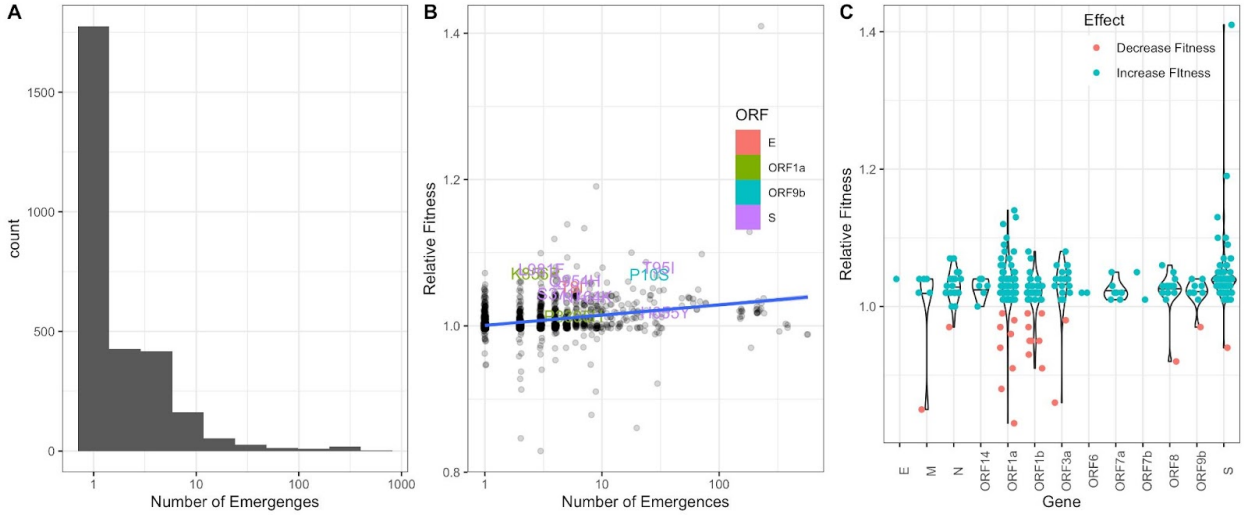


**Figure S8. A.** Histogram of the number of independent emergences across all observed mutations. A mutation was considered to have emerged independently if it was present in a lineage but not in its parent. **B.** Scatterplot of the fold-change in fitness versus the number of independent emergences. The top 10 ranked mutations are labeled, colored by ORF. Linear regression with standard error for the slope given as shaded area. **C.** Violin plots of fold-change in fitness for mutation, grouped by gene. The top 10% most statistically significant mutations are shown (where significance is determined by z-score of the approximate variational posterior).

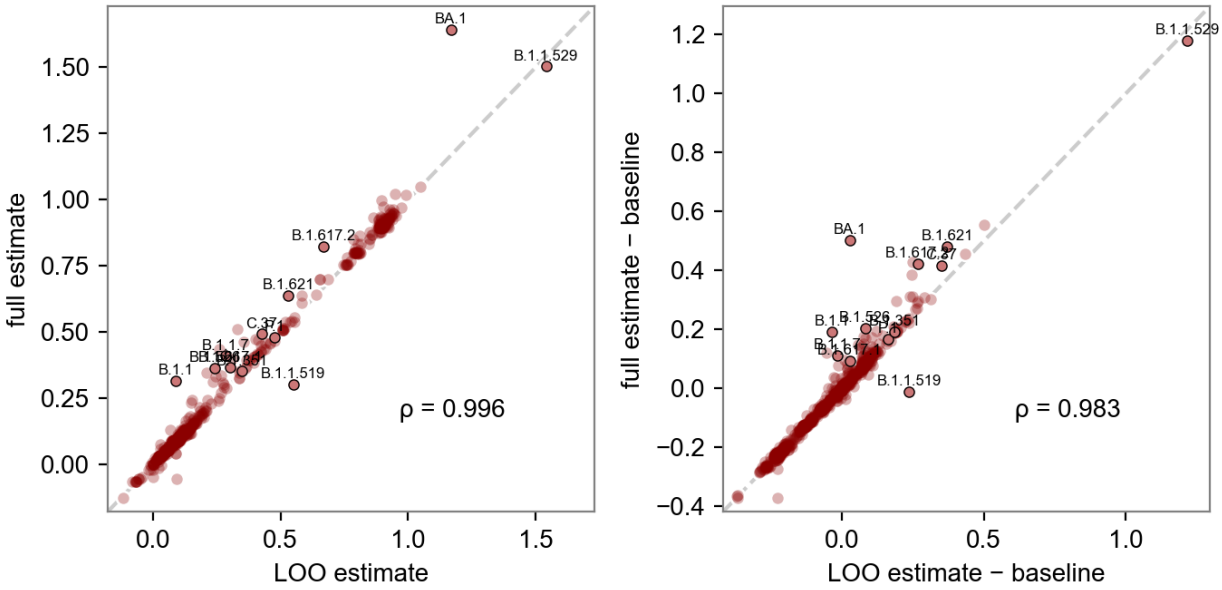


**Figure S9.** Accuracy of predicted fitness based solely on mutation content. **Left:** estimated $\log(R/R_A)$ for each lineage based on the full set of GISAID samples (y axis), and on the leave-one-out subset with each lineage's subclade removed and the fitness estimated from the mutations present in the lineage (x axis). **Right:** the same quantities but relative to a baseline estimator in which each child lineage's fitness is the same as that of its parent lineage. If a mutation is entirely removed from the LOO dataset, then the corresponding mutation coefficient is estimated as zero. The evaluation metrics are Pearson correlation (ρ) and mean absolute error (MAE). The MAE of the leave-one-out estimator is 0.001, more than 100x smaller than the MAE of the baseline estimator (0.129). Both panels highlight the CDC's variants of concern and variants of interest. The lineages selected for testing are those with at least 100 samples and with the largest deviations from their parent, i.e. where the baseline estimator performs worst. Note that the fitness of child lineages can deviate substantially from that of the parent, e.g. BA.1 is surprisingly higher fitness than its parent B.1.1.529.

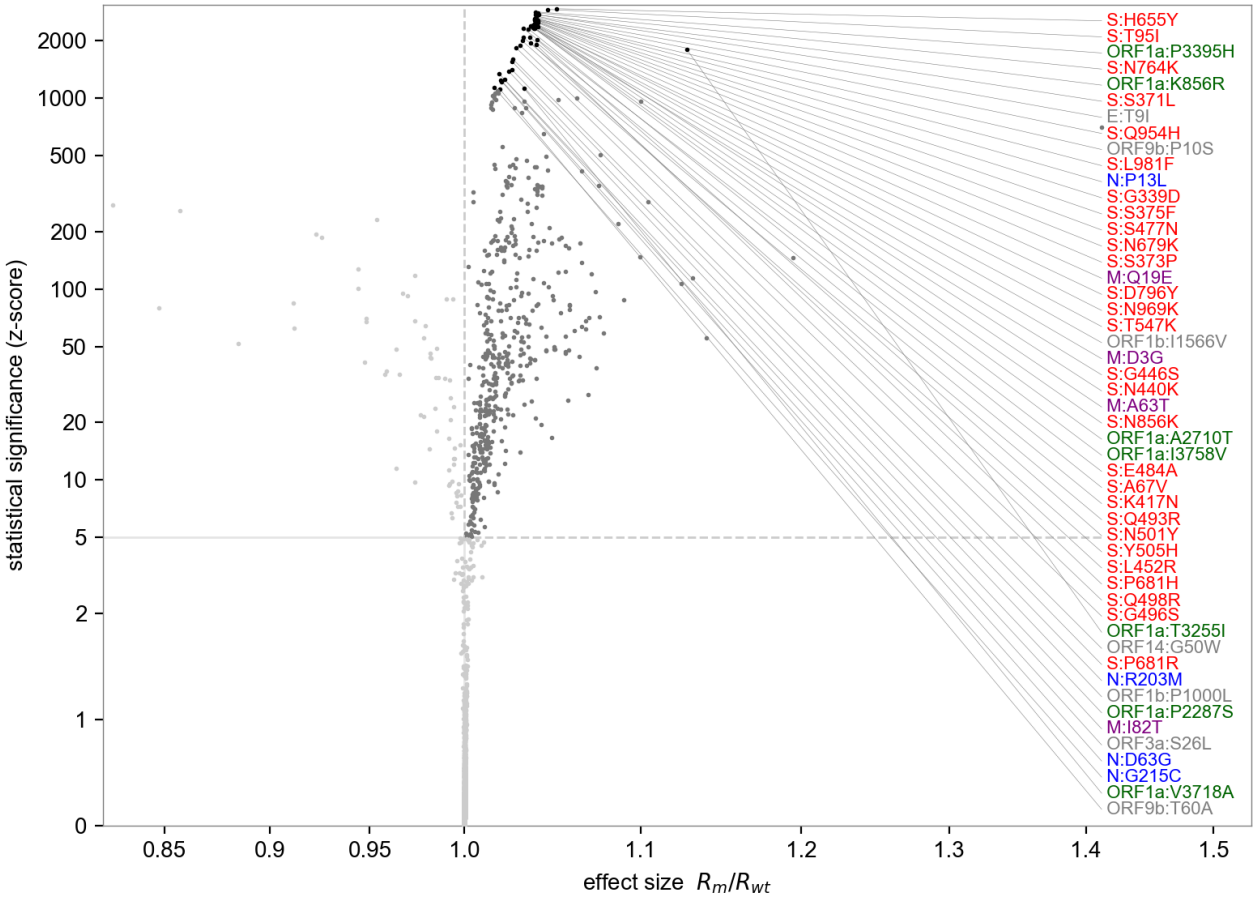


**Figure S10.** Volcano plot highlighting the most statistically significant mutations linked to increased fitness. The x-axis depicts the effect size as a ratio of estimated fitness of lineages with-versus-without each mutation. The y-axis depicts z-score from the approximate variational posterior as a proxy for statistical significance. The top 50 most statistically significant mutations are labeled, colored by gene. The 540 growth-associated mutations with z-score greater than 5 are shaded dark gray.

A.

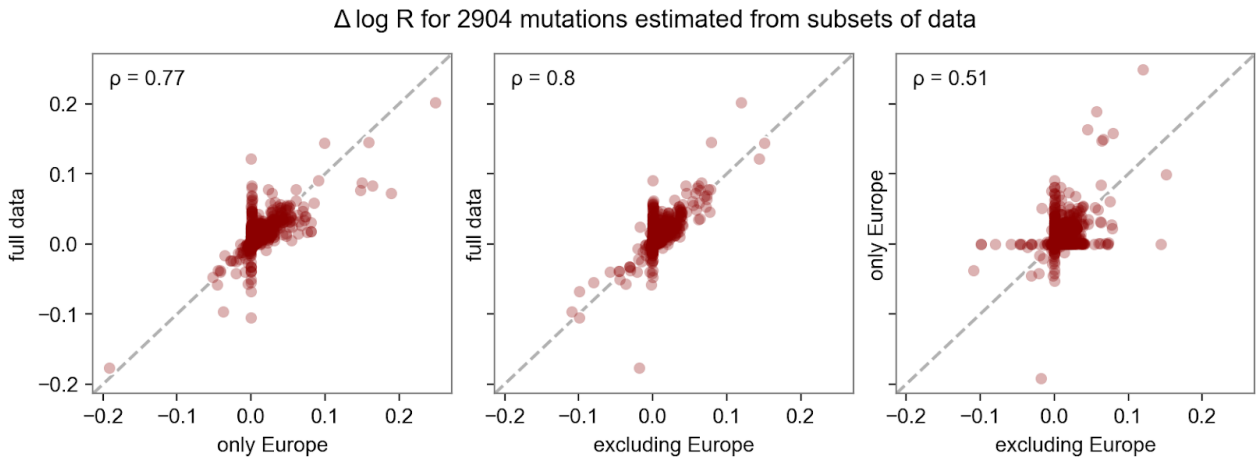


B.

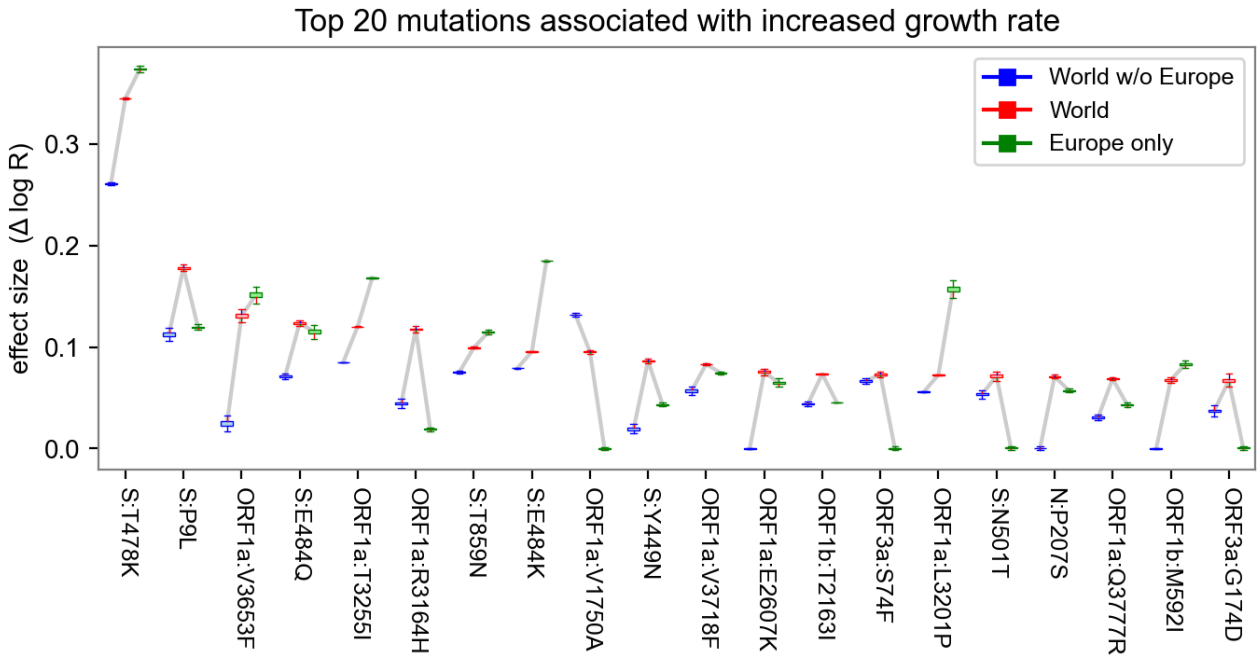


C.

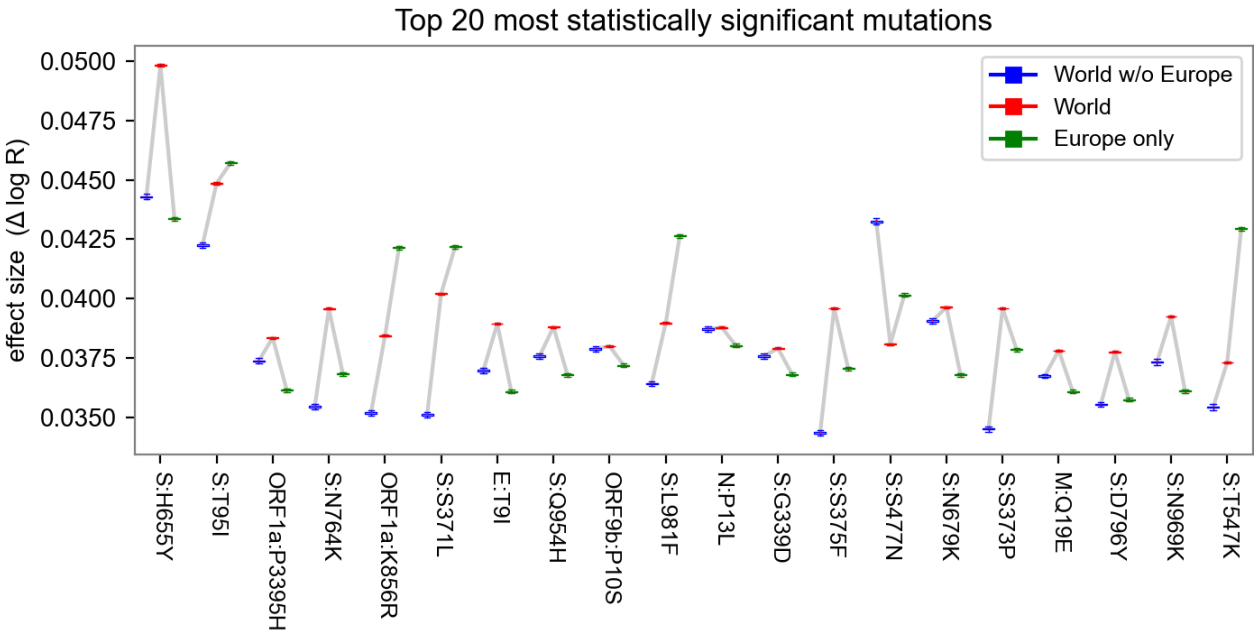


**Figure S11.** Sensitivity of mutation estimates. **A.** Scatterplot of the mutation coefficients on the full model and geographic subsets, with Pearson correlation (ρ) as shown. **B.** Box-and-whisker plot depicting estimated growth rates with corresponding uncertainties for the 20 lineages with highest growth rate (effect size) across geographic subsets. **C.** Same as B but with the top 20 lineages sorted by statistical significance (z-score). Note that in B, the World estimates (center) tend to be higher than subsets (left and right) only because the ranked selection is based on those estimates.

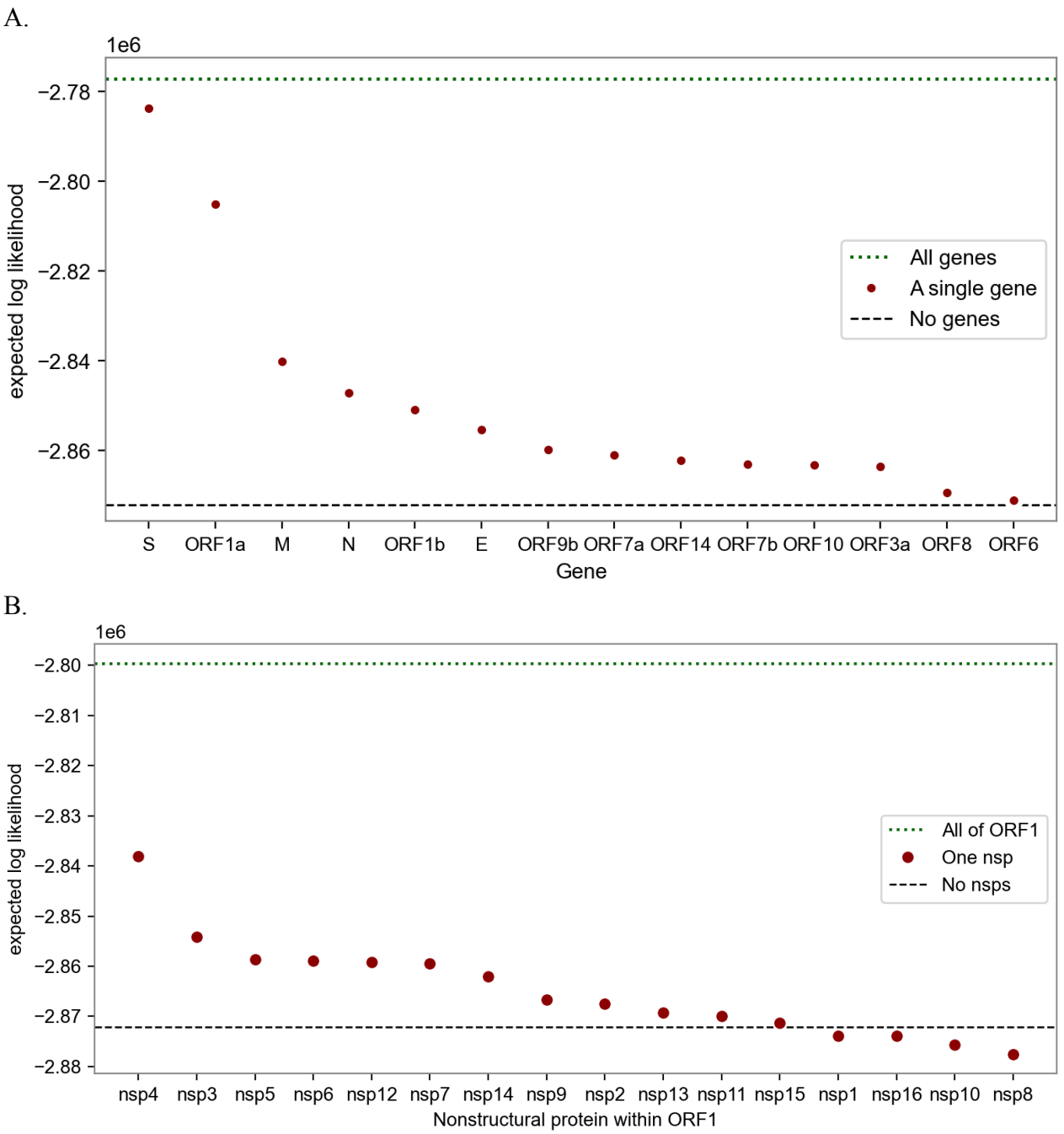


**Figure S12.** Information content of different subsets of the SARS-CoV-2 genome in explaining fitness. The metric is the expected log likelihood. The dotted line at the top shows the performance of the full model that regresses against all genes (A) or against all of ORF1 (B). The circles show estimators based on only single genes (A) or single nonstructural proteins (B). The most informative genes are S, ORF1a, M, N, and ORF1b; within ORF1 the most informative nsps are nsp4, 3, 5, 6, 12 and 7. The bottom dashed lines show the performance of a naive estimator that ignores genetic information, effectively estimating each lineage's growth rate in each region independent of growth rate estimates in other regions.

A.

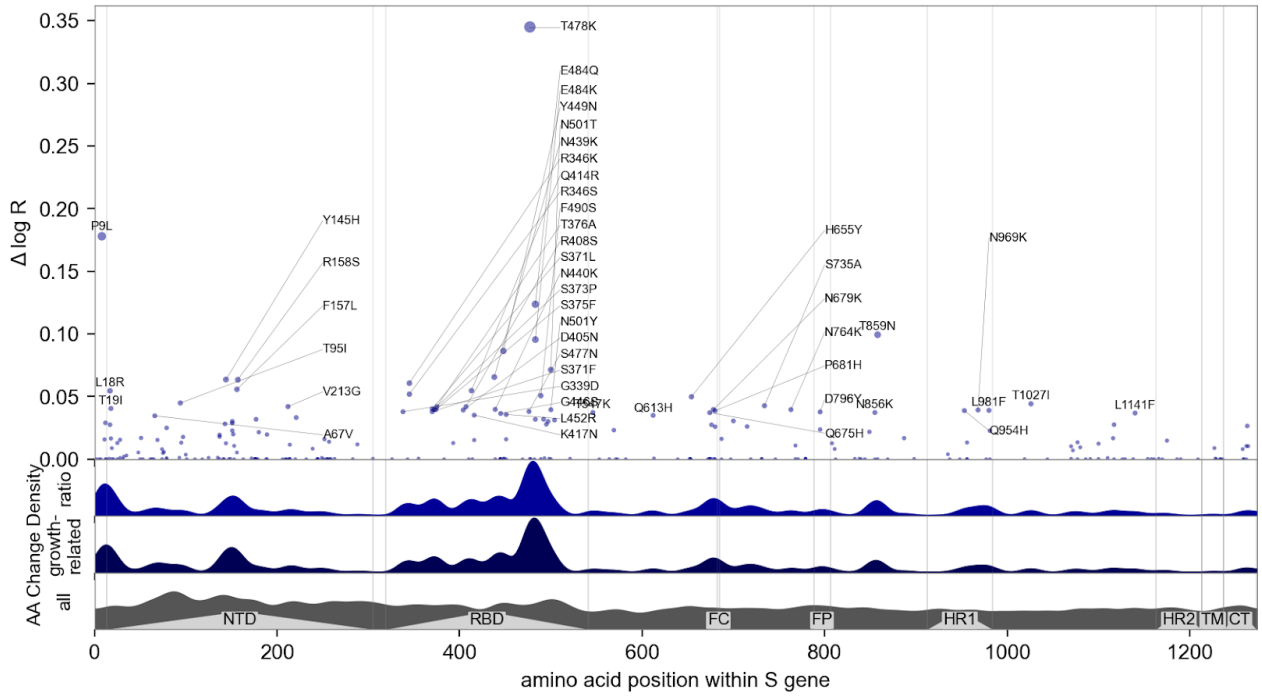


B.

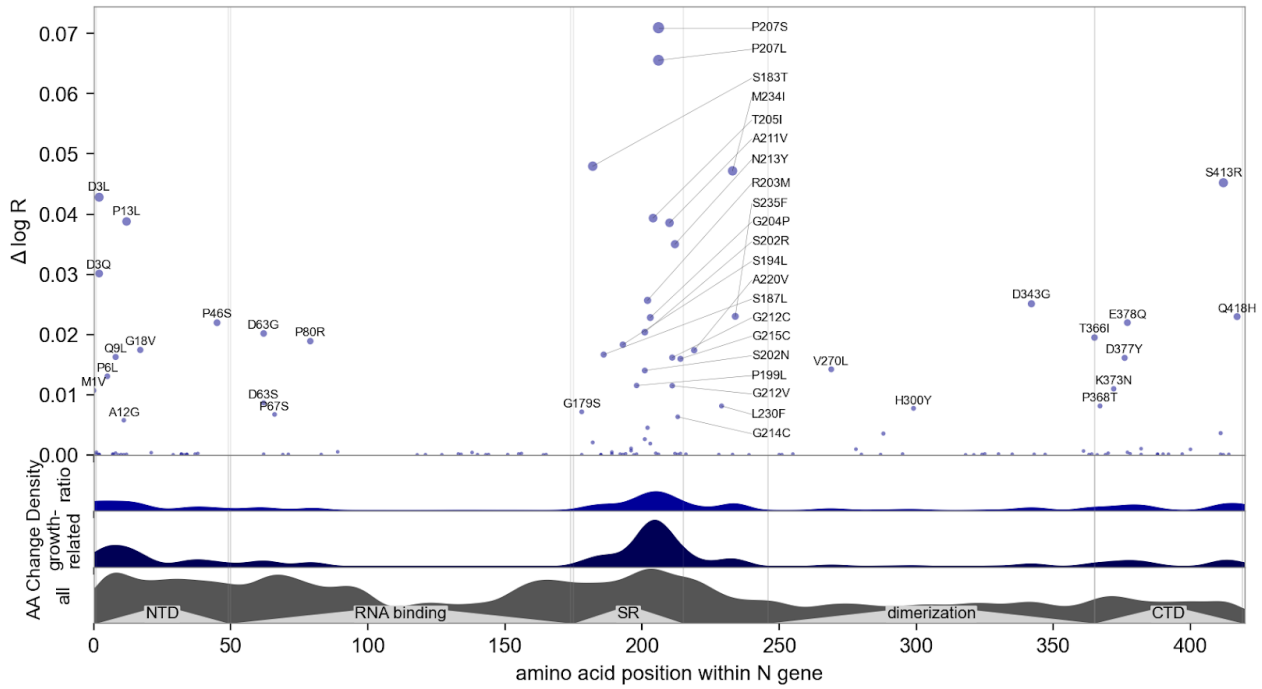

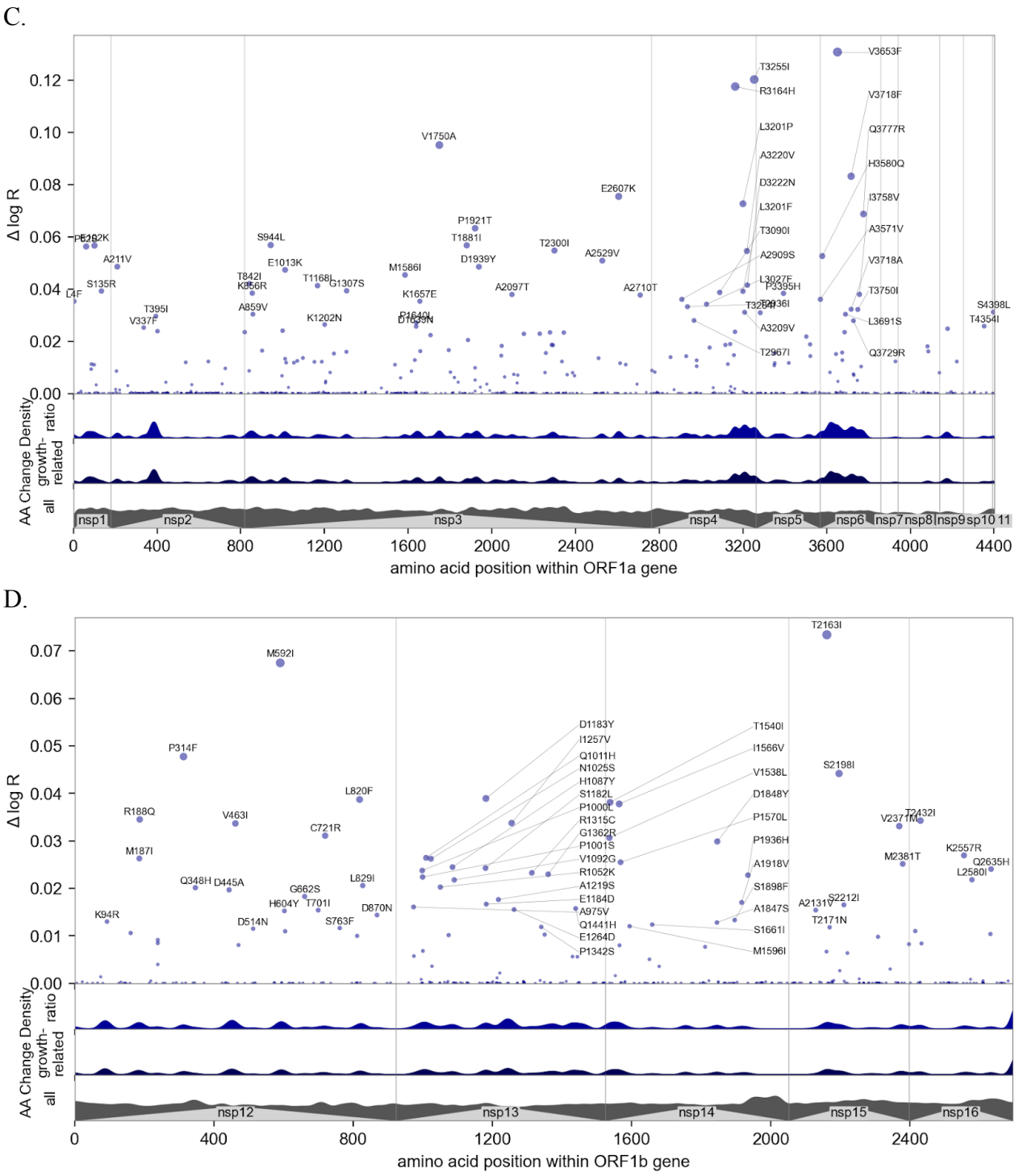


**Figure S13.** Manhattan plot details of the four most informative genes. See Figure 3 for a whole-genome view and Figure S12 for ranking by information. **A.** View of the 1237 amino acids of the S protein, annotated by structure (*45*); many mutations occur in the N-terminal domain (NTD), receptor-binding domain (RBD), and furin cleavage (FC) site. Regions containing the fusion peptide (FP), heptad repeat (HR) 1 and 2, transmembrane domain (TM), and C-terminal domain (CTD) are annotated. **B.** View of the 419 amino acids of the nucleocapsid (N) protein domains, annotated by structure (*46*); many mutations occur in the serine–arginine rich region (SR), identified by (*47*) as immunogenic. **C.** View of the ORF1a

polyprotein, including 11 non-structural proteins (nsps). **D.** View of the ORF1b polyprotein, including nsp12-16; note the amino acid positions do not account for 9 additional residues at the N-terminus of nsp12 (RNA polymerase) resulting from the -1 ribosomal frameshift.

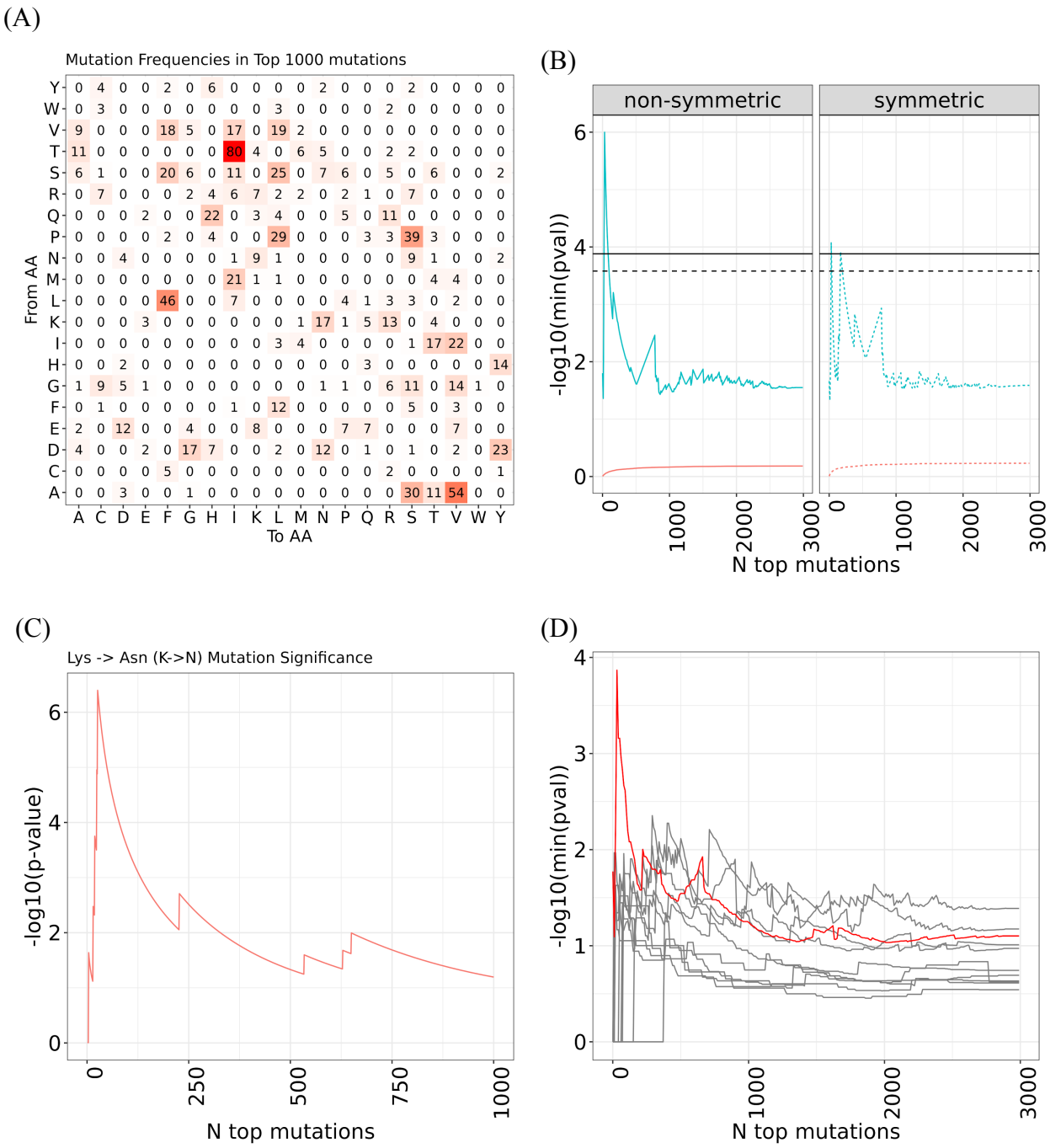


**Figure S14**: Enrichment analysis of amino acid changes among top-ranked mutations **A.** Mutation frequency in top 1000 most significant mutations (as ranked by posterior mean/stddev) **B.** Leading set enrichment analysis of most significant mutations predicted by the model for non-symmetrical (e.g. A->V) (left) and symmetrical (e.g. A<->V) (right) amino acid changes. The blue curve depicts the most significant p-value obtained for different top-N mutation cutoff values across all amino acid changes, while the red curve depicts the mean p-value. **C.** Further examination reveals that top mutations are enriched in K to N changes in the S gene. **D.** No other genes (gray) other than S (in red) show significant enrichment.

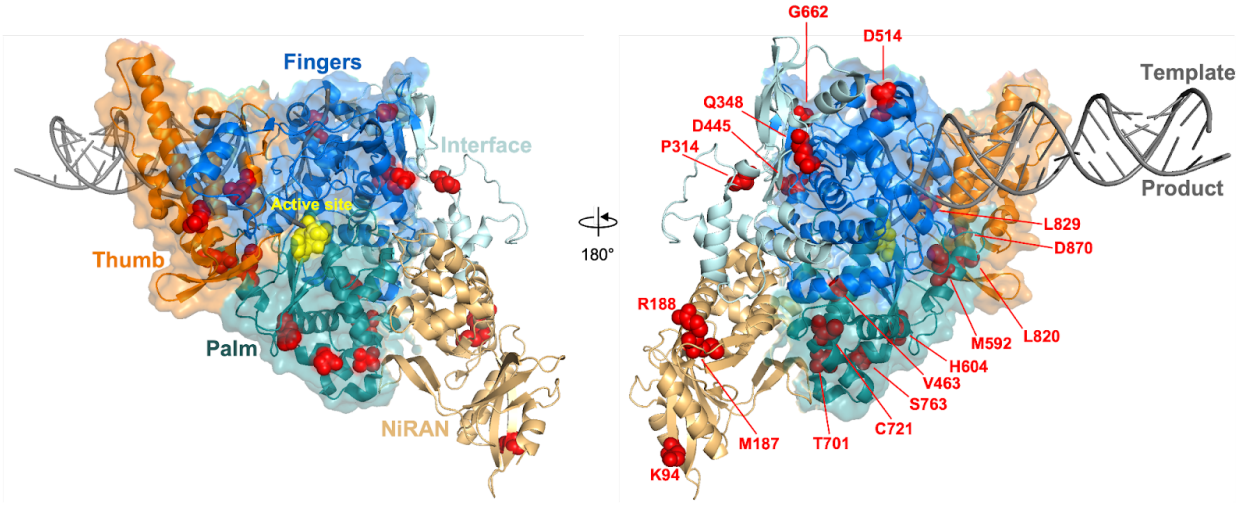


**Figure S15.** Top-ranked mutations in the viral RNA-dependent RNA polymerase (RdRP, nsp12, PDB: 7CYQ). Amino acid positions corresponding to top mutations are shown as red spheres. The catalytic site residues 750-SDD-752 are highlighted as yellow spheres. The coronavirus-specific domains (NiRAN, Interface) are shown as cartoon structures. The conserved RdRP domains (Fingers, Palm, Thumb) are shown as cartoon and surface filling structures.

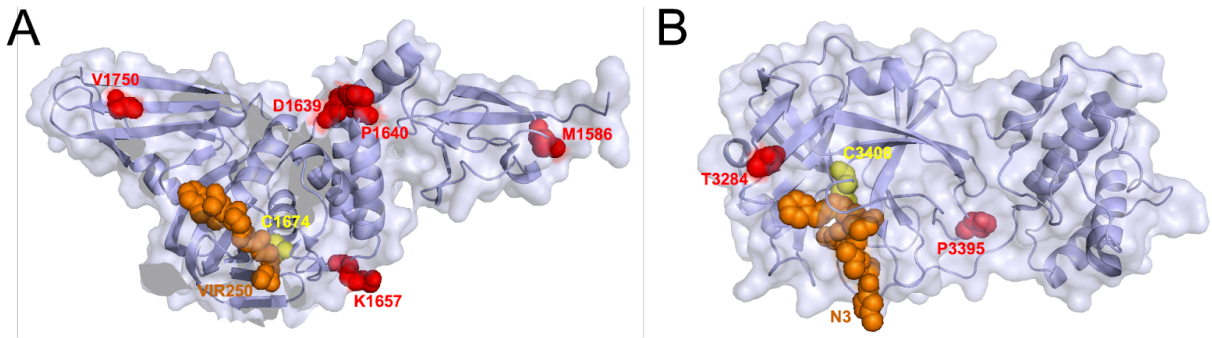


**PLpro** (nsp3, PDB: 6WUU) **M$^{pro}$** (nsp5, PDB: 6LU7)

**Figure S16**. Top-ranked mutations in the two viral proteases, PLpro (A) and M$^{pro}$ (B). Both protease structures are shown in light blue. Amino acid positions corresponding to top mutations are shown as red spheres. The catalytic cysteine residues for each are shown as yellow spheres. Two active-site inhibitors, VIR250 and N3, are shown as orange spheres.

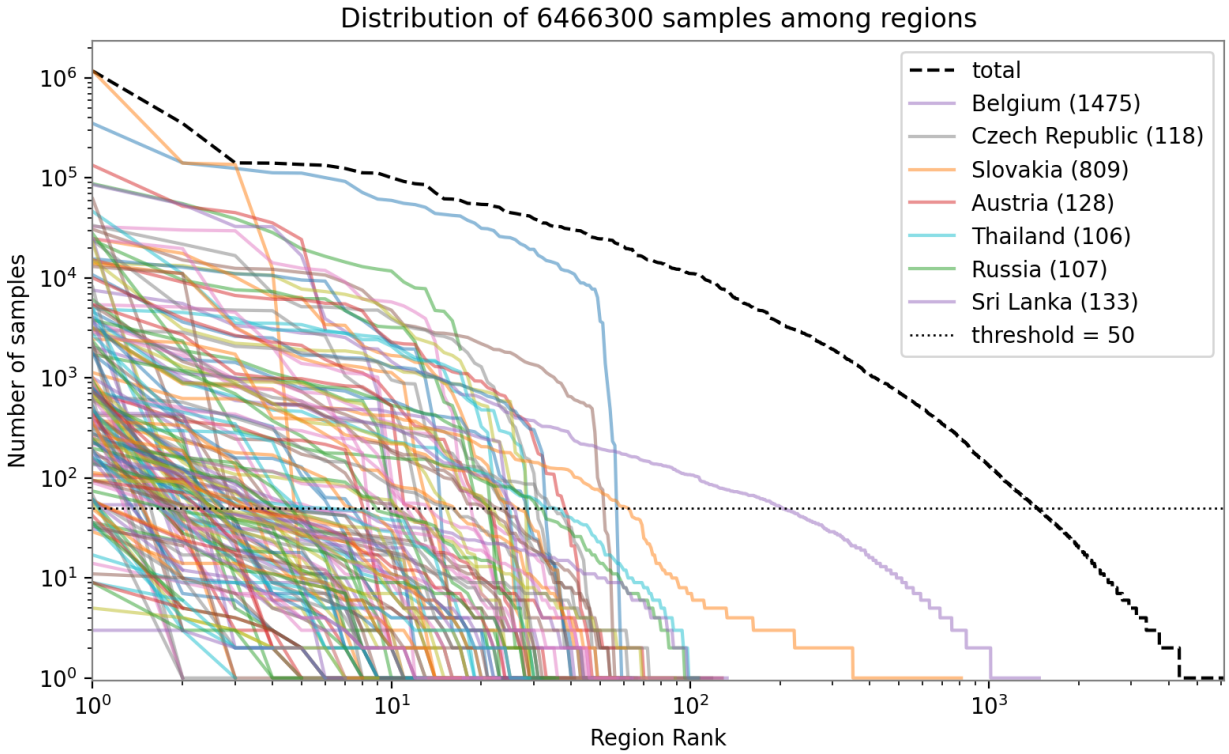


**Figure S17.** Distribution of samples among regions. Each 2nd level GISAID region (country) is plotted as a curve, with the sizes of 3rd level GISAID regions (usually provinces or states) plotted as points along the curve. The 3rd level is dominated by a few countries with many small regions (e.g. Belgium with 1475 regions), so we merge regions smaller than a threshold (50 samples) into their respective countries.

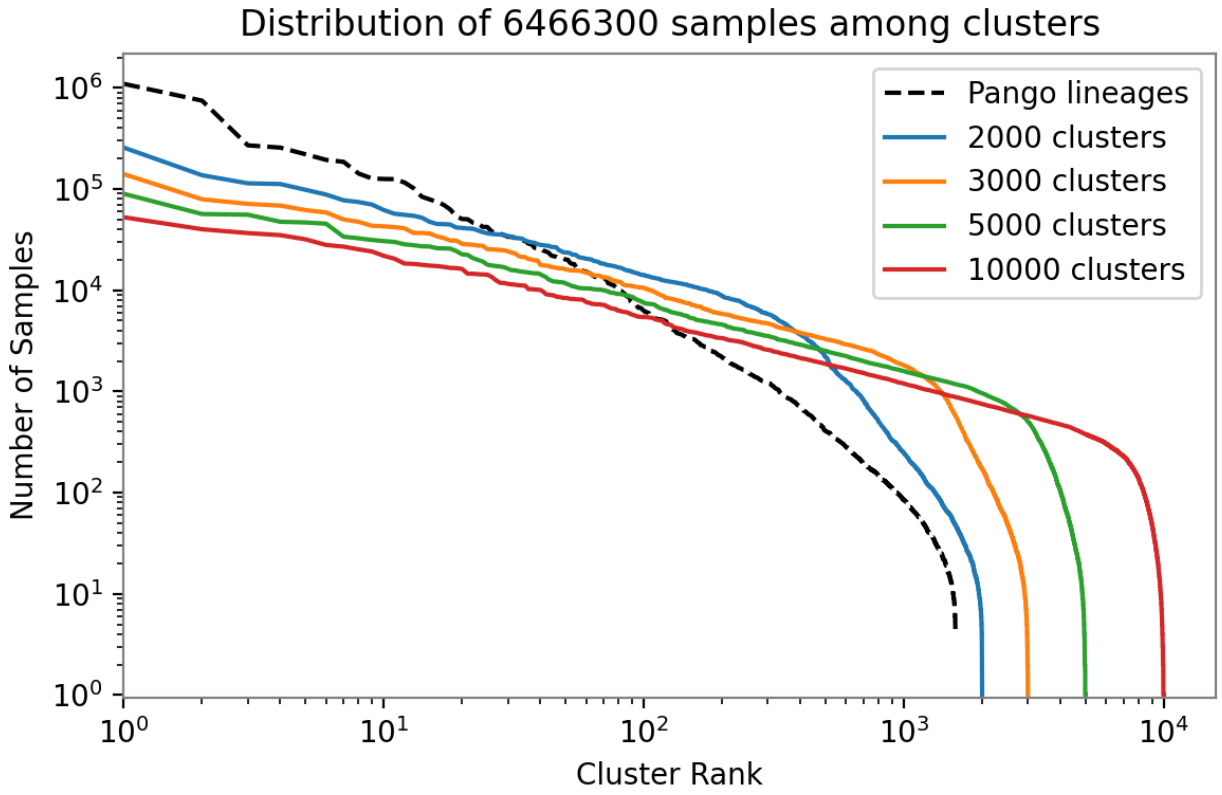


**Figure S18.** Distribution of samples among PANGO lineages and refined clusters. PANGO lineage sizes are heavy-tailed and appear heterogeneous, so we split into a larger number of clusters (colored). We chose a final clustering of 3000 clusters (orange), balancing between a smaller number of clusters (which improves statistical efficiency) and a larger number of clusters (which better represents lineage heterogeneity).

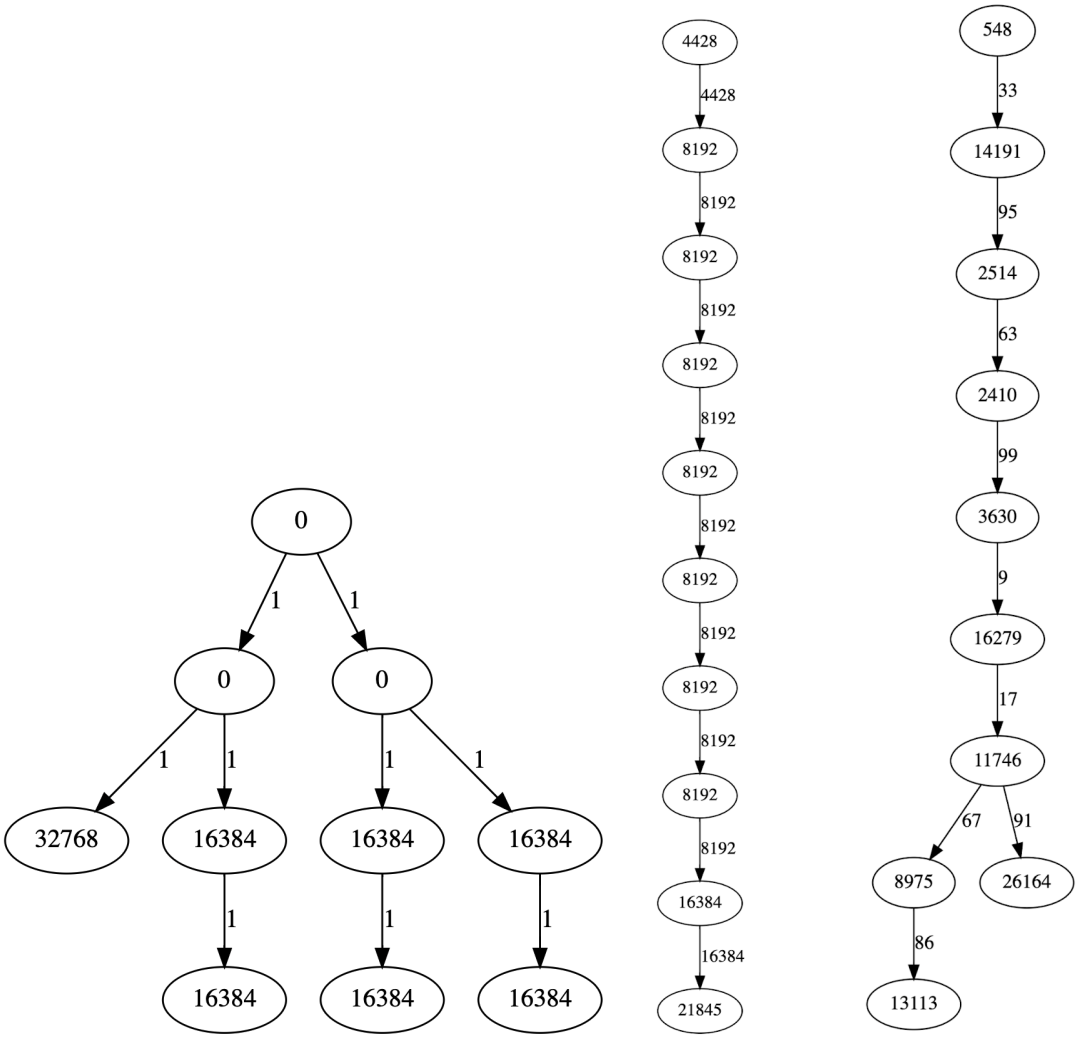


A. B. C.

**Figure S19:** Example algorithmic clustering of three synthetic trees. Example synthetic mutation annotated trees are clustered into smaller trees with only 10 nodes. Nodes are annotated by the number of sequences represented by each cluster. Edges are annotated by the edit distance between clusters. (A) clusters a balanced binary tree of 262,143 nodes, (B) clusters a single linear chain of 20,001 nodes, (C) clusters a random binary tree with Geometric(½)-many children at each node and 200,000 nodes. In all examples the clustered trees are approximately balanced insofar as they exhibit narrow distributions of edge distances (in SNPs) and the cluster sizes (in genomes sampled).

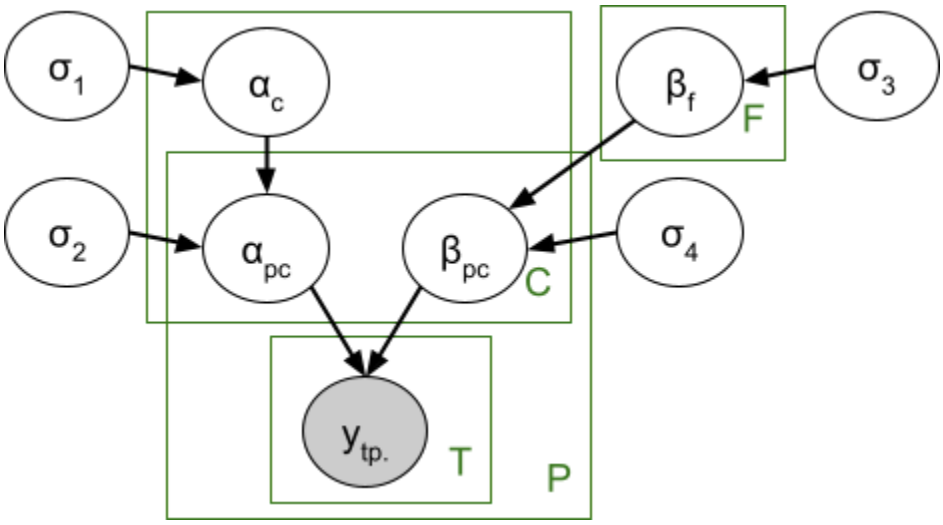


**Figure S20.** Probabilistic graphical model structure of the $PyR_0$ model. Variables σ are scale parameters of distributions. Variable $\beta_f$ is the per-amino-acid-substitution fitness coefficient. Variables $\beta_{pc}$ and $\alpha_{pc}$ are respectively the per-region per-cluster slope and intercepts parametrizing multivariate logistic growth curves. The mean parameter of $\beta_{pc}$ is determined by $\beta_f$ via matrix multiplication by the feature matrix $X_{cf}$. The mean parameter of $\alpha_{pc}$ is a per-cluster intercept $\alpha_c$ shared across regions. The multinomial observations are vectors $y_{tp.}$ each of whose entries $y_{tpc}$ is the number of samples of cluster c in place p in time bucket t. Green boxes denote plates, i.e. conditionally independent replicas of random variables. Note the vector-valued observation $y_{tp.}$ is outside of the C plate because the multinomial distribution couples entries across the cluster coordinate c. Because the P x C plates are sparse (in most places most clusters never appear) the model omits $\alpha_{pc}$ and $\beta_{pc}$ for pairs (p,c) with no observations in y.

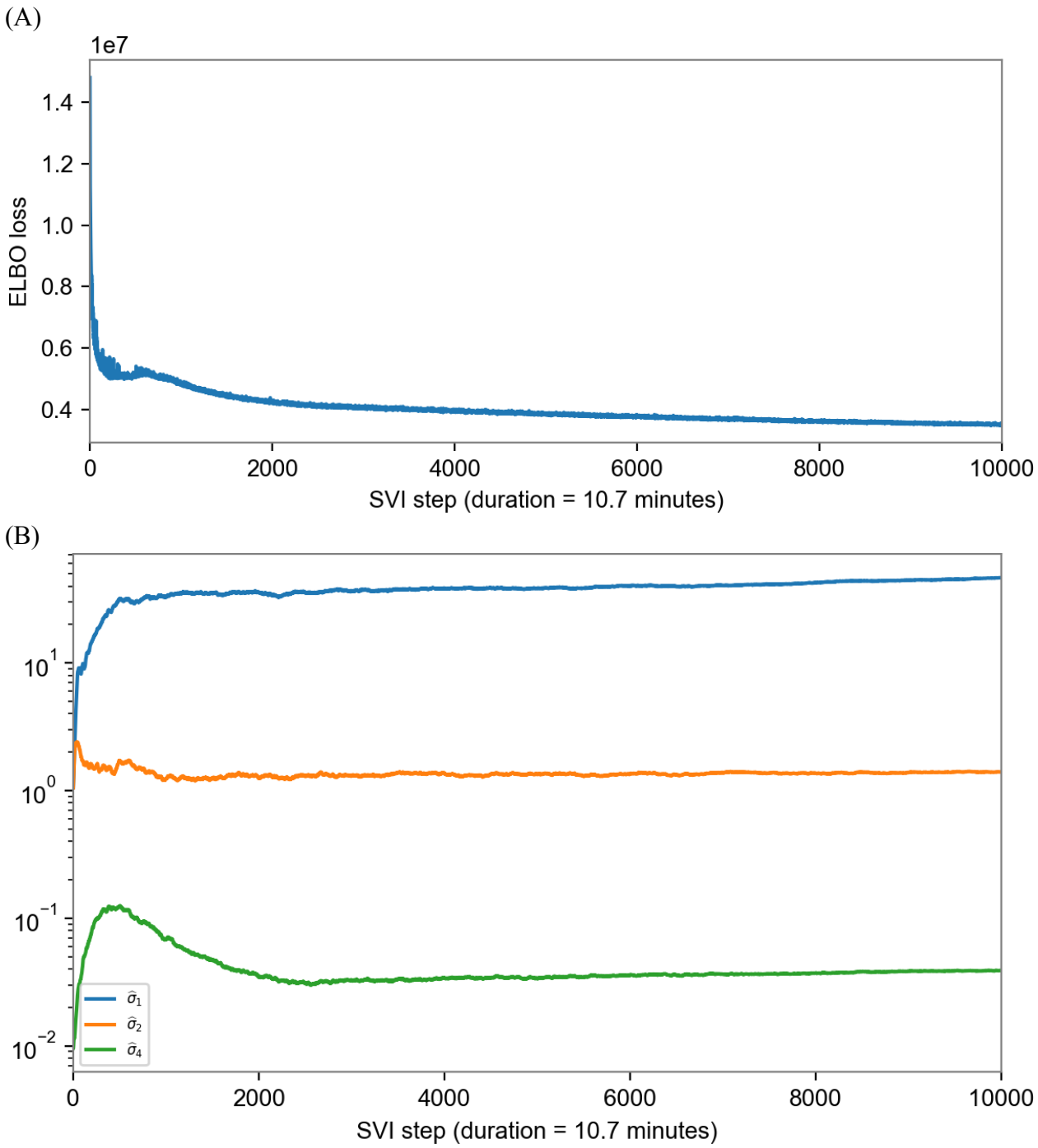


**Figure S21.** Convergence of variational inference algorithm. **A.** Convergence of ELBO loss. **B.** Convergence of posterior medians of scale parameters.

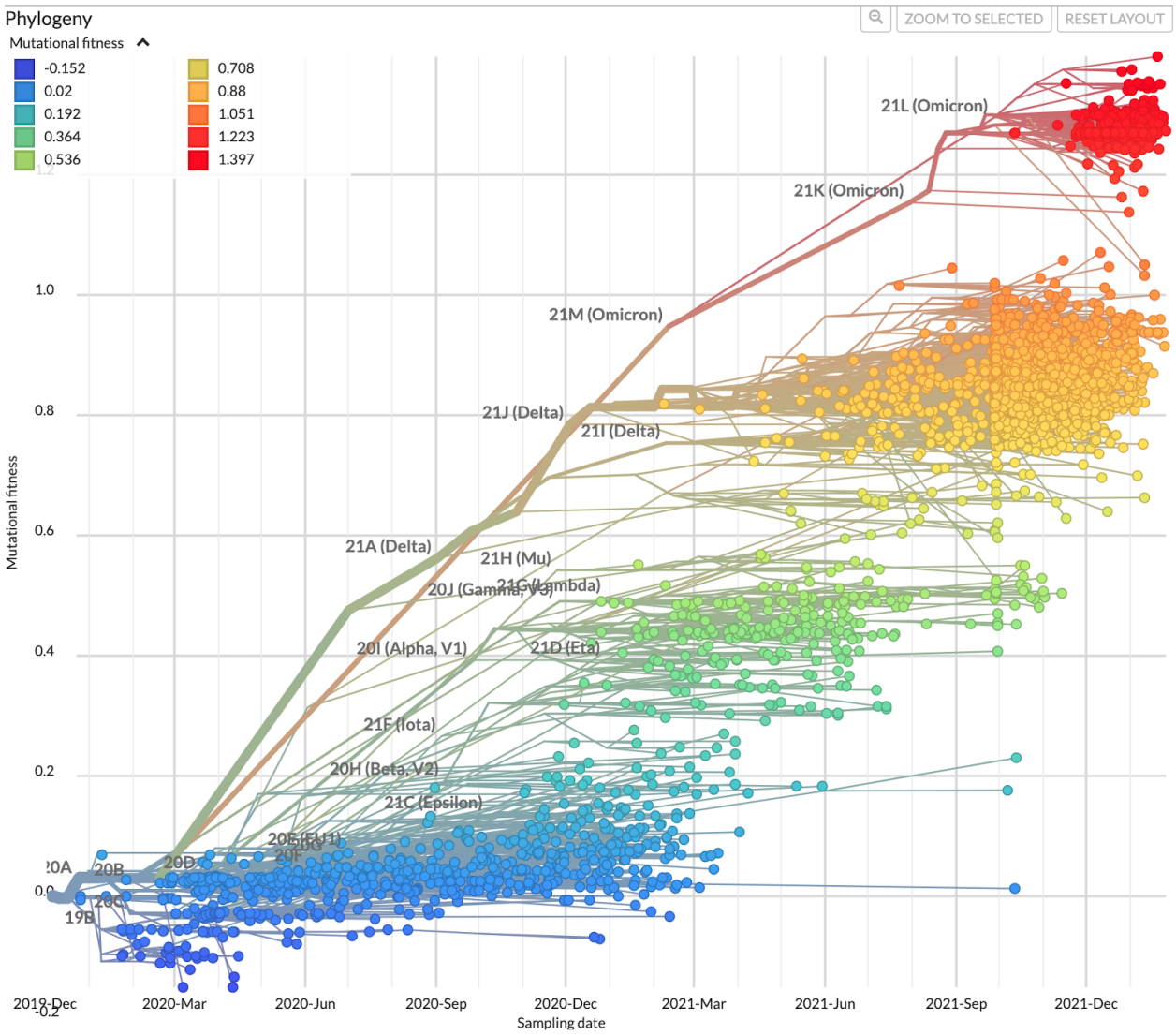


**Figure S22:** Screenshot of https://nextstrain.org displaying Nextstrain's subsampled phylogeny with color and y-axis (mutational fitness) determined by our model predicted Δ log R for each lineage (here using a slightly older version of our model). Although $PyR_0$ does not explicitly rely on phylogenetic information, fitness estimates vary smoothly across the phylogeny.

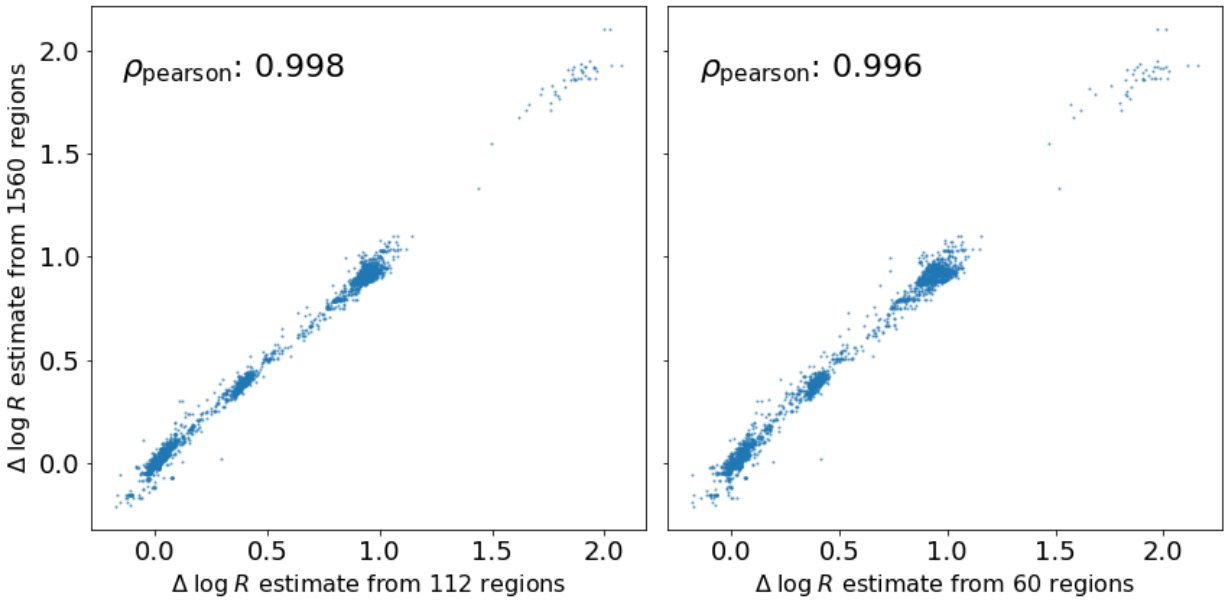


**Figure S23**. We show that $PyR_0$ lineage-level Δ log R estimates are largely driven by regions with the largest numbers of samples, as would be expected from a Bayesian hierarchical model. The vertical axis depicts Δ log R estimates based on all 1560 regions, while the horizontal axis on the left (respectively, right) depicts Δ log R estimates based on the 112 (60) regions with at least $10^4$ ($2 \times 10^4$) samples. Collectively these regions contain 80.7% (69.8%) of the total number of SARS-CoV-2 sequences in our full dataset.

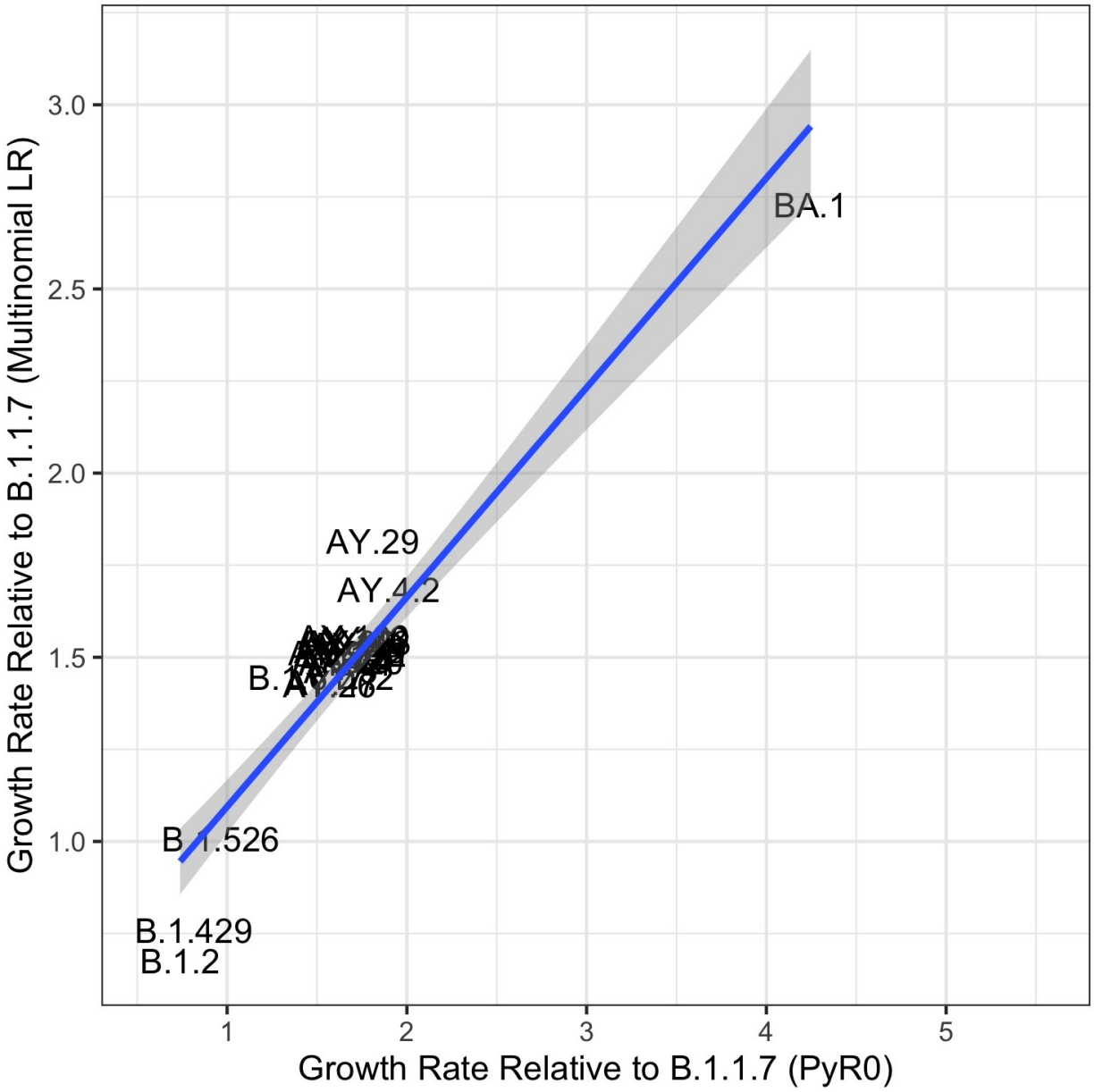


**Figure S24**. Comparison of mutation-level regression coefficients for growth rate among 50 most prevalent lineages using a standard multinomial logistic regression model with estimates of lineage growth rates from $PyR_0$. Pearson's R = 0.95.

A.

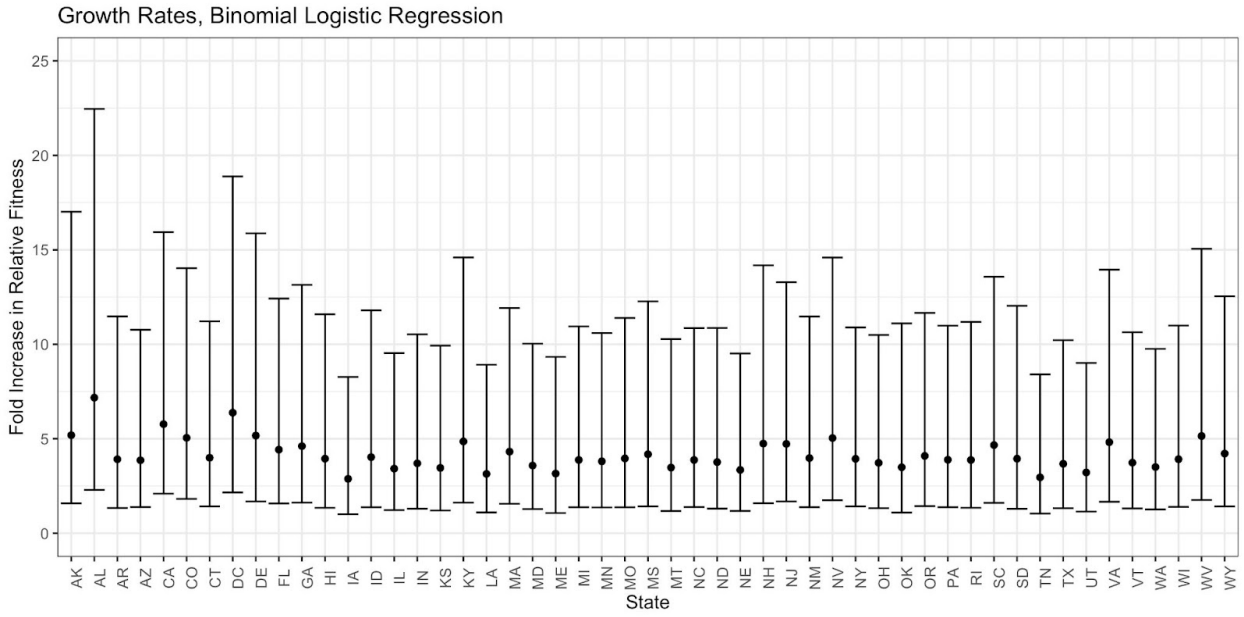


B.

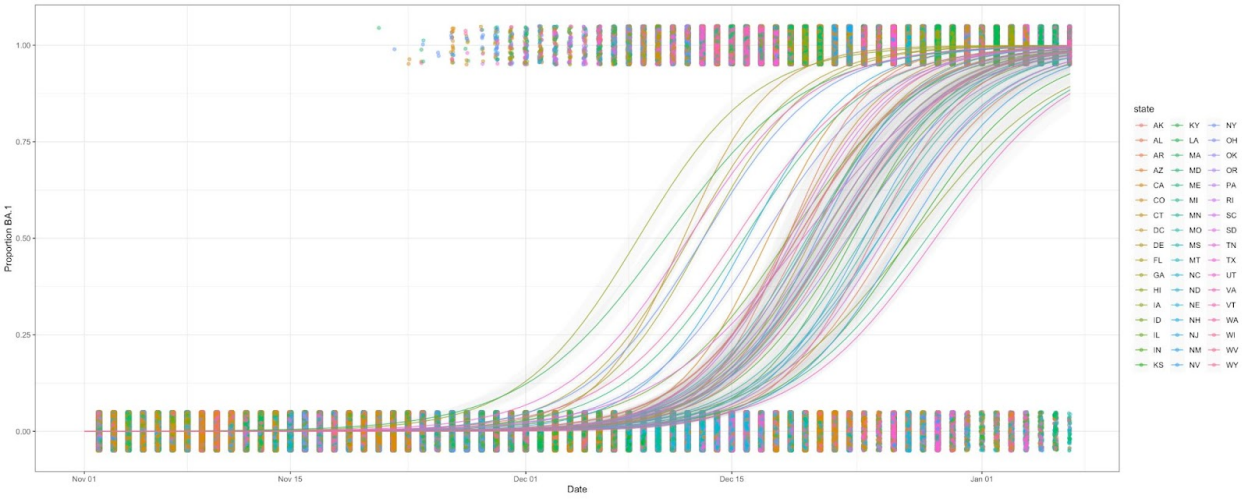


**Figure S25**. **A.** Estimated growth rate per viral generation (5.5 days) in each state using binomial logistic regressions for the emergence of BA.1 against a background consisting of Delta (B.1.617.2 and sublineages) viruses in all 50 US states between November 1 2021 and January 7 2022. Fold increase in relative fitness is expressed as $\exp(\boldsymbol{\beta}_1)$, where time is measured in viral generations. Error bars show $\exp(\boldsymbol{\beta}_1 +/- SE(\boldsymbol{\beta}_1))$. For all 50 US states, the median growth rate per viral generation of Omicron over Delta was 3.9. For all states, the confidence interval for the binomial logistic regression coefficient contained the estimate for the ratio of Omicron to Delta from the $PyR_0$ model, which was 3.1 for BA.1.1 / B.1.617.2 and 2.8 for BA.1 / B.1.617.2. **B.** Estimated probability of BA.1 by state from the binomial logistic regression.

| Region | 4-week forecast | 8-week forecast |
|---|---|---|
| USA | 82.9% | 68.3% |
| France | 75.6% | 61.0% |
| England | 75.6% | 58.5% |
| Brazil | 65.9% | 51.2% |
| Australia | 56.1% | 39.0% |
| Russia | 73.2% | 68.3% |

**Table S1.** Regional evaluation of forecasts. We evaluate the ability of $PyR_0$ to accurately forecast the dominant lineage 4- and 8-weeks into the future in six selected regions with a relatively large number of GISAID samples. Percentage accuracies are obtained by averaging over 45 training windows.

| Spatial region | # of mutations | Extent of region (nt) | p-value | Lengthscale |
|---|---|---|---|---|
| Entire genome | 2904 | 29394 | 0.000001 | 100 |
| Entire genome | 2904 | 29394 | 0.000001 | 500 |
| S | 415 | 3786 | 0.001910 | 50 |
| N | 220 | 1251 | 0.017627 | 50 |
| ORF7a | 75 | 360 | 0.024066 | 18 |
| ORF3a | 198 | 789 | 0.024307 | 39 |
| ORF1a | 1107 | 13182 | 0.029710 | 50 |
| ORF7b | 26 | 126 | 0.089589 | 6 |
| ORF14 | 69 | 213 | 0.112527 | 11 |
| ORF6 | 19 | 177 | 0.138634 | 9 |
| ORF1b | 552 | 8052 | 0.329416 | 50 |
| E | 17 | 195 | 0.455606 | 10 |
| M | 42 | 639 | 0.518497 | 32 |

**Table S2.** Spatial structure of the inferred amino acid coefficients $\beta_f$. We report one-sided p-values for the Moran I spatial autocorrelation statistic computed using a permutation test. We use a gaussian weighting function of the form $\exp(-\text{distance}^2/\text{lengthscale}^2)$, where distance is measured in units of nucleotides. We find that there is significant evidence for spatial structure in S, N, ORF7a, ORF3a, and ORF1a as well as across the SARS-CoV-2 genome as a whole.

| Open Reading Frame (ORF) | Rank | Mutation | Fold Increase in Transmissibility | Number of Lineages |
|---|---|---|---|---|
| Nucleocapsid | | | | |
| | 11 | P13L | 1.04 | 26 |
| | 42 | R203M | 1.03 | 214 |
| | 47 | D63G | 1.02 | 209 |
| | 48 | G215C | 1.02 | 152 |
| | 57 | D377Y | 1.02 | 228 |
| | 70 | D3L | 1.04 | 13 |
| | 82 | Q9L | 1.02 | 8 |
| | 83 | S413R | 1.05 | 3 |
| | 91 | S235F | 1.02 | 15 |
| ORF1b | | | | |
| | 21 | I1566V | 1.04 | 6 |
| | 43 | P1000L | 1.02 | 221 |
| | 53 | G662S | 1.02 | 212 |
| | 58 | A1918V | 1.02 | 152 |
| | 71 | L829I | 1.02 | 9 |
| | 72 | T2163I | 1.08 | 3 |
| | 75 | I1257V | 1.03 | 3 |
| | 78 | H1087Y | 1.02 | 5 |
| | 80 | T1540I | 1.04 | 6 |
| Spike | | | | |
| | 1 | H655Y | 1.05 | 34 |
| | 2 | T95I | 1.05 | 31 |
| | 4 | N764K | 1.04 | 7 |
| | 6 | S371L | 1.04 | 4 |
| | 8 | Q954H | 1.04 | 6 |
| | 10 | L981F | 1.04 | 3 |
| | 12 | G339D | 1.04 | 5 |
| | 13 | S375F | 1.04 | 6 |
| | 14 | S477N | 1.04 | 48 |

**Table S3.** Table of the most statistically significant mutations in spike, ORF1b, and nucleocapsid. The top 9 mutations for each of the listed ORFs is shown. Mutations such as S:H655, S:T95I, and N:R203M have emerged independently in VoC lineages.

**Data S1.** (separate file strains.tsv)
Complete list of PANGO lineages with inferred relative fitness, ranked by fitness.
Mirrored at https://github.com/broadinstitute/pyro-cov/blob/v0.2/paper/strains.tsv

**Data S2.** (separate file mutations.tsv)
Complete list of amino acid changes with inferred effect size, ranked by z-score.
Mirrored at https://github.com/broadinstitute/pyro-cov/blob/v0.2/paper/mutations.tsv

**Data S3.** (separate file accession_ids.txt.xz)
Complete list of GISAID accession numbers of viral genomes used in this study.
Mirrored at https://github.com/broadinstitute/pyro-cov/blob/v0.2/paper/accession_ids.txt.xz